Synthesis of 2D Layered Perovskite $Cs_4CuSb_2Cl_{12}$ Nanocrystal and Their Sunlight Driven Photocatalysis Reaction

Deepraj Verma

A dissertation submitted for the partial fulfilment of BS-MS dual degree in Science

Indian Institute of Science Education and Research (IISER) Mohali
April, 2021

Certificate of Examination

This is to certify that the dissertation titled **"Synthesis of 2D Layered Perovskite $Cs_4CuSb_2Cl_{12}$ Nanocrystal and Their Sunlight Induced Photocatalysis Reaction"** submitted by **Mr. Deepraj Verma** (Reg. No. MS16120) for the partial fulfillment of the BS-MS dual degree programme of the Institute, has been examined by the thesis committee duly appointed by the Institute. The committee finds the work done by the candidate satisfactory and recommends that the report be accepted.

Dr. Angshuman Roy Choudhury
(Local/Administrative Guide)

Dr. Santanu Kumar Pal

Dr. Subhabrata Maiti

Debrina Jana

30.04.21

Dr. Debrina Jana
(Supervisor)

Dated: April 30, 2021

Declaration

The work presented in this dissertation has been carried out by me under the guidance of Dr. Debrina Jana at the Indian Institute of Science Education and Research Mohali. This work has not been submitted in part or in full for a degree, a diploma, or a fellowship to any other university or Institute. Whenever contributions of others are involved, every effort is made to indicate this clearly, with due acknowledgment of collaborative research and discussions. This thesis is a Bonafide record of original work done by me, and all sources listed within have been detailed in the bibliography.

Deepraj Verma

Deepraj Verma

(Candidate)

Dated: April 30, 2021

In my capacity as the supervisor of the candidate's project work, I certify that the above statements by the candidate are true to the best of my knowledge.

Debrina Jana

30.04.21

Dr. Debrina Jana

(Supervisor)

Acknowledgements

I am indebted to my Institute Indian Institute of Science Education and Research Mohali for providing me with the opportunity for higher education and research. I thank DST-INSPIRE for providing my fellowship.

I would also like to express my sincere gratitude to my Supervisor, Dr. Debrina Jana, her guidance and valuable support throughout this work.

I gratefully acknowledge INSPIRE faculty research grant of Dr. Debrina Jana and the National allocation fund of IISER Mohali for funding this work. I am thankful to IISER Mohali central facility for doing TEM and SEM.

I would like to express my sincere gratitude to my Local/Administrative guide Dr. Angshuman Roy Choudhury, project committee members Dr. Santanu Kumar Pal, and Dr. Subhabrata Maiti for reviewing my thesis and offer me valuable feedback.

I am thankful to the Department of Chemical Sciences for providing a departmental teaching laboratory and other experimental and computational facilities.

I would like to acknowledge the Library and computer centre for their continuous support to provide access to any paper and internet, email, respectively. I am also thankful to the stores and purchase section for their timely efforts and the dean's academics office to maintain our academic records and make our study period smooth. I am thankful to the members of my lab group for their support and friendliness - in particular, Ms. Ashitha, Ms. Saumya Sebastian,

Ms. Neha Bajaj, Mr. Akhilesh Kumar Meena, Mr. Mrinal Kanti, Mr. Mayank Joshi, Ms. Labhini Singla, and Mr. Sachin Jadhav.

Last but not least, I owe my deepest gratitude to my parents and family members for everything I am and anything I shall ever be. I sincerely thank all my friends who supported me throughout this duration. They are too numerous to be all named individually, but I must mention those whose contributions have been immensely impactful. My sincere regards to Aritra Bhattacharya, Aaditya Mishra, Pravin, Madhusudan Maity, Rahul Singh Yadav, Umakant Gaurav, Yuvraj Vaishnav, Himanshu Meena, Sarvdev Jaiswal, Harsh Kishor, Monu, Naveen kumar Baghel for helping me out in difficult situations. Lastly, I would like to mention Aritra Bhattacharya again for generously allowing me to use his workstation and for the innumerable fruitful discussions. This dissertation would not be existing in its present state without him.

Deepraj Verma

List of Figures

Figure 1. Cubic perovskite structure of ABX_3 (figure reproduced from Ref. 3)..... 1
Figure 2. Different reported structures of metal halide perovskites (copyright permission from Ref. 14) 6
Figure 3. The cubic crystal structure of 3D Lead halide perovskite(figure reproduced from Ref. 37) . 7
Figure 4. Crystal structures of **(a)** 3D perovskite**, (b)** (001) 2D perovskite (N-MPDA) [$PbBr_4$], and **(c)** (110) 2D perovskite (copyright from Ref. 37)..... 8
Figure 5. Schematic layered organic-inorganic halide perovskites. R is an organic group, sheets (copyright permission from Ref. 43)..... 8
Figure 6. Schematic of the main processes in a photocatalytic reaction (figure reproduced from Ref. 49) 12
Figure 7. Schematic diagram of Band structure..... 13
Figure 8. Hot injection synthesis of 2D Layered $Cs_4CuSb_2Cl_{12}$ NCs..... 20
Figure 9. Acid-mediated solution-phase synthesis 2D Layered $Cs_4CuSb_2Cl_{12}$ MCs 21
Figure 10. Compares the XRD patterns of synthesized $Cs_4CuSb_2Cl_{12}$ NCs to the JCPDS results at different scaled-up batches[66]..... 23
Figure 11. (a)UV-Vis spectrum and **(b)** Tauc plot of $Cs_4CuSb_2Cl_{12}$ NCs[66] 23
Figure 12. (a)-(c) He1 UP spectral scan of DPCl1 **(d)** Schematic diagram of Band structure of DPCl1 24
Figure 13. X-band EPR spectra for Cu^{2+} in DPCl1 NCs at room temperature 25
Figure 14. Ferricyanide photocatalytic reduction setup..... 27
Figure 15. (a) UV-visible spectra of conversion of Fe^{3+} to Fe^{2+} **(b)** Corresponding kinetic plots, **(c)** Digital image of colour transition**, d)** Depicted picture of band positions of catalyst (DPCl1) NCs[66] 28
Figure 16. (a) The rate constants for the ferricyanide reduction reaction up to 4 cycles using DPCl1**, (b)** PXRD of the reused catalyst in comparison with JCPDS data for $Cs_4CuSb_2Cl_{12}$[66]..... 29
Figure 17. (a) Dye degradation reaction setup and **(b)** UV-visible spectral change, kinetics, colour transition of Congo red[66] 30
Figure 18. (a) UV-visible spectra of Congo red dye solution in presence of DPCl2 photocatalyst under sunlight, **(b)** corresponding first-order kinetic plot 31
Figure 19. Mechanism of congo red dye degradation reaction..... 33
Figure 20. Degradation rates for Congo red dye with photocatalyst, radical scavengers, and under dark..... 34
Figure 21. Development of fluorescent peak at 455 nm in the photocatalytic reaction mixture of 1 mg/ml of DPCl1 photocatalyst, 10^{-4} M coumarin, and **(a)**various concentration of Ag^+ under sunlight, **(b)** 2×10^{-4} M $AgNO_3$, and various concentration of oxalic acid under sunlight[66] 35
Figure 22. Synthesis of BACl (butylammonium chloride) salt..... 38
Figure 23. (a) Synthesis of undoped $(BA)_2PbCl_4$ NCs, **(b)** colorless undoped $(BA)_2PbCl_4$ NCs 38
Figure 24. (a) Synthesis of Cu^+ doped $(BA)_2PbCl_4$ NCs, Cu^{2+}doped crystals in **(b)** normal light, digital image in UV light of **(c)** at wavelength 365, **(d)** at wavelength 254nm 39
Figure 25. Tauc plot of **(a)** Undoped $(BA)_2PbCl_4$, **(b)** Cu^+, **(c)** Cu^{2+} doped $(BA)_2PbCl_4$ 41
Figure 26. DSC Analysis of **(a)** undoped $(BA)_2PbCl_4$, **(b)** Cu doped $(BA)_2PbCl_4$ 41

Figure 27. UPS Analysis of (**a)** undoped $(BA)_2PbCl_4$, **(b,c,d)** Cu^{2+} doped $(BA)_2PbCl_4$.....42
Figure 28. UV-visible spectral change of Congo red dye solution in presence of Cu^{2+} doped $(BA)_2PbCl_4$ photocatalyst under sunlight, inset corresponding kinetic plot, colour transition 44
Figure 29. UV-visible spectra of Congo red dye solution in presence of Cu^{2+} doped $(BA)_2PbCl_4$ and t- butyl alcohol (hydroxyl scavenger) under sunlight, inset corresponding kinetic plot.....45
Figure 30. Congo red dye degradation **(a)** without photocatalyst in the presence of sunlight **(b)** with photocatalyst in dark.....45
Figure 31. (a) Degradation rates for Congo-red dye using photocatalyst Cu^{2+} doped $(BA)_2PbCl_4$ in dark, sunlight, hydroxyl radical scavengers **(b)** mechanism of dye degradation 47

List of tables

Table 1: Comparison of apparent ferricyanide reduction constants with hot injection catalysts with other photocatalysts from previous literature. 29
Table 2: Comparison of apparent rate constants rate of congo red dye degradation with hot injection catalysts with other photocatalysts from previous literature..... 31

Notations

PSC	Perovskite Solar Cell
PCE	Photo Conversion Efficiency
HPs	Halide perovskites
NCs	Nanocrystals
DPs	Double perovskites
VBM	Valence Band Maximum
CB	Conduction band
AFM	Atomic Force Microscopy
DSC	Differential Scanning Calorimetry
EDX	Energy-Dispersive X-Ray Spectroscopy
FTIR	Fourier-Transform Infrared Spectroscopy
MCs	Microcrystals NCs Nanocrystals
PXRD	Powder X-Ray Diffraction
TEM	Transmission Electron Microscopy
TGA	Thermogravimetric Analysis
UPS	Ultraviolet Photoelectron Spectroscopy
UV	Ultra-violet
XPS	X-ray Photoelectron Spectroscopy
BG	Band Gap
A	Acceptor
D	Donor

Contents

List of Figures ..... **i**
List of tables ..... **iii**
Notations ..... **iv**
Abstract ..... **ix**
Chapter 1 ..... **1**
Introduction **1**
1.1 Perovskites 1
1.1.1 Historical background 2
1.1.2 Properties 3
1.2 Different synthetic method of perovskites 3
1.2.1 Solid-state Reactions 3
1.2.2 Hot injection method 4
1.2.3 Solution phase synthesis 4
1.2.4 Gas-phase preparations 4
1.2.5 Mesoporous-mediated synthesis 4
1.3 Lead-free halide perovskites 5
1.4 Lead halide perovskites 6
1.4.1 Ruddlesden–Popper 2D Lead Halide Perovskite 7
1.5 Usage of perovskites as a photocatalyst 9
1.5.1 Principles of heterogeneous photocatalysis 11

1.5.2 Mechanisms of the Photocatalytic Process for wastewater treatment..... 12
1.5.3 Role of different scavengers in heterogeneous photocatalysis 15
1.6 Current Work 17
1.7 Instrumentation..... 18
Chapter 2.....19
Project 1. Synthesis of 2D layered $Cs_4CuSb_2Cl_{12}$ double perovskite and its photocatalytic activity.....19
2.1 Materials 19
2.2 Synthetic Protocol of $Cs_4CuSb_2Cl_{12}$ double perovskite 20
2.2.1 Synthesis of 2D layered $Cs_4CuSb_2Cl_{12}$ NCs via hot injection method ... 20
2.2.2 Synthesis of 2D $Cs_4CuSb_2Cl_{12}$ NCs via acid-mediated solution-phase method21
2.3 Results and Discussion 22
2.4 Application of $Cs_4CuSb_2Cl_{12}$ as photocatalyst 25
2.4.1 Introduction 25
2.5 Photocatalysis experiments 27
2.5.1 Photocatalytic reduction of ferricyanide 27
2.5.2 Congo Red dye degradation reaction..... 30
2.5.3 Principle and Mechanism of Congo Red dye degradation Reaction..... 32
2.5.4 Using coumarin as a fluorescent probe for hydroxyl radical 34
(˙OH) detection..... 34
Chapter 3.....37
Project 2. Copper doping on 2D perovskite $(BA)_2PbCl_4$ and its photocatalytic activity 37
3.1 Materials 37
3.2 Synthesis of undoped $(BA)_2PbCl_4$ and Cu^+, Cu^{2+} doped $(BA)_2PbCl_4$ 37
3.2.1 Synthesis of undoped $(BA)_2PbCl_4$..... 37
3.2.2 Synthesis of Cu^+ and Cu^{2+} doped $(BA)_2PbCl_4$..... 39
3.3 Result and discussion..... 40
3.4 Application of Cu^{2+} Doped $(BA)_2PbCl_4$ double perovskite as photocatalyst. 43
3.4.1 Introduction 43
3.4.2 Photocatalytic degradation of congo red dye 43

Conclusions and Future Outlook 48
Conclusions 48
Project 1 48
Project 2 48
Future Outlook 49
Bibliography 50

Abstract

Perovskite nanocrystals have emerged as a potential candidate in the field of heterogeneous catalysis as photocatalysts as well as in a plethora of optoelectronic applications. In recent years, lead-based halide perovskites have been developed with excellent electrical and optical properties; however, concerns about their stability and toxicity have motivated the search for alternatives. The research is pioneered to synthesize lead-free halide double perovskites to overcome both issues simultaneously. The synthesis of 2D layered $Cs_4CuSb_2Cl_{12}$ NCs using a simple hot injection synthetic method is carried out. The material is thereafter characterized using various techniques like UV-Vis spectroscopy, PXRD, UPS, EPR, TGA, DSC, AFM, TEM, etc. The layered perovskites show a promising bandgap for photocatalytic activity. For the first time, the productive photocatalytic behaviour of these Pb-free NCs against metal-centered ferricyanide redox and Congo red dye degradation reactions is demonstrated.

Additionally, research on copper doping in 2D $(BA)_2PbCl_4$ and their application in photocatalysis is carried out. Characterizing studies (PXRD, UV-Vis spectroscopy, DRS, UPS, TGA, DSC) are undertaken to reveal the formation and properties of the doped materials. Subsequently, a variety of photocatalytic reactions is carried out using scavengers.

.

Chapter 1

Introduction

1.1 Perovskites

Perovskites are compounds with the structural formula ABX_3, where A, B, and X represent cations and anion. Most A^+ is monovalent with the stoichiometry, and divalent B^{2+} ions will form a complex halide perovskite ABX_3 (if X = Halogen group elements).[1] A perovskite structure is, in general, a three-dimensional arrangement of corner-sharing octahedral BX_6 units with the A ion sandwiched between the cuboctahedra interstices.[2]

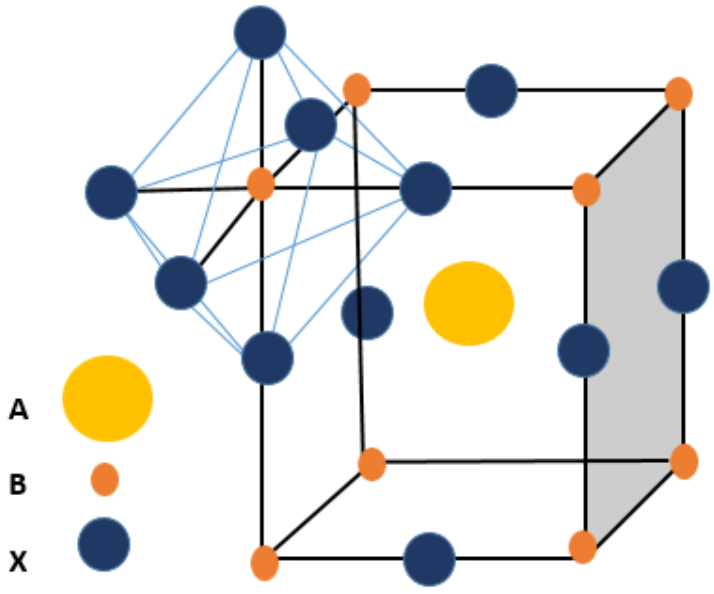

Figure 1. Cubic perovskite structure of ABX_3 (figure reproduced from Ref. 3)

The Goldschmidt tolerance factor (t) is commonly used to estimate the stability of perovskite structure using the chemical formula, ABX_3, and the ionic radius, 'r', of each ion.[4] Alternatively, providing information on the compatibility of ions with a crystal structure. Almost all the reported perovskites reported to date have the tolerance factor and octahedral factor values in the range of $0.81 < t < 1.11$ and $0.38 < \mu < 0.89$**,** respectively.

$$t = \frac{r_A + r_B}{\sqrt{2(r_A + r_B)}} \qquad \mu = \frac{r_B}{r_X}$$

Here, r_A and r_B denote the A and B site cations' ionic radii, respectively, and r_X represents the anion's ionic radius. The ionic radii of A, B, and X must satisfy the following tolerance and octahedral factors. A tolerance factor evaluates whether the A-site cation is going to fit inside the BX_3 framework's cavities.

The tolerance factor value decides the structure types as

1. If t = 1 means the possibility to shape a perfect cubic cell.
2. If t > 1 implies the chance to shape lower dimensions.

Octahedral factor value decides the stability of BX_6 octahedra and should be greater than 0.377 ($\mu > 0.377$) to form perovskites; otherwise, it doesn't form perovskites phases.[5]

1.1.1 Historical background

Halide perovskites emerge with a fantastic incomparable property due to their morphology and stability towards different challenging conditions, making them unique in applying solid-state perovskite solar cell (PSC) and their photocatalytic properties with high power-conversion efficiency (PCE); research on perovskite photovoltaics has increased previously unseen and exponentially. Presently, approved PCE for perovskite solar cells reaches 22.7 %, surpassing traditional thin-film solar cell PCEs.[6]

Organic-inorganic halide perovskites based on Lead have emerged as possible candidates in the field of optoelectronics and energy resource applications. However, due to their low

stability in polar solvents and the lead toxicity, The use of HPs as sunlight-driven catalysis is still a significant problem.[7] A perfect photocatalytic material should have many desirable physical properties, including large and strong light absorption, efficient charge separation, long operational stability, and sufficient redox capacity for target reactions.[8]

1.1.2 Properties

Halide perovskites have interesting physical and chemical properties such as large optical transmission domains, high resistivity, antiferromagnetic, extraordinary magnetic, piezoelectric, photoluminescent properties, anionic conductivity, a wide temperature range, dielectric, low exciton binding energies, piezoelectric behaviour, and lower bandgap with tunability.[9,10] Halide perovskites are thermally more stable and exhibit several intriguing chemical properties in heterogeneous catalytic action. For example, these NCs are often used to efficiently reduce CO_2 levels in the atmosphere and transform CO_2 into value-added chemicals and fuels, thus contributing to renewable energy and meeting the rise in energy demand. These materials are also used to degrade complex environmental contaminants.[11]

1.2 Different synthetic method of perovskites

Different methods for synthesizing halide perovskites compounds have reported producing various materials that show various commercial and technical application and a wide range of magnetic, electrical, optical, and mechanical properties over a wide range of temperature. Several methods such as; Solid-state reactions, Solution-phase synthesis, Hot injection method, Gas-phase preparations were attributed for synthesizing perovskites compounds.[12]

1.2.1 Solid-state Reactions

It is a mechanochemical process that doesn't require any solvent or high-temperature treatment. All non-volatile solid chemicals mixed thoroughly in the stoichiometric amount, which reacts to form the product needed.[13]

1.2.2 Hot injection method

The hot injection method is widely used for the synthesis of metal halide perovskite. It requires the rapid injection of a hot solution of one precursor into the mixture of hot solvents and capping agents to create a homogeneous solution.[14] The capping ligands that are present in the reaction medium prevent the nanocrystals from being agglomerated. After nucleation, a homogeneous controlled growth throughout the mixture is observed, with larger NCs increasing more slowly than smaller NCs, resulting in a size-focusing effect. The hot-injection approach is beneficial because it allows for precise control throughout particles morphology by allowing for immediate nucleation separate from the growth stage.[15]

1.2.3 Solution phase synthesis

Solution phase synthesis was the first and only process for producing peptides, but many researchers now use it to perform several organic reactions and synthesize various perovskite materials. Solution-phase synthesis often results in a mixture of products in a single container. For this reason, there has been a lot of interest in solution phase synthesis. This approach's key drawback is the difficulty in removing unnecessary impurities at each stage of the synthesis.[16]

1.2.4 Gas-phase preparations

All gas-phase preparation methods have fundamental molecular nuclei formations, followed by subsequent condensation and coalescence, generating the nanoparticles in high-temperature regions via continuous growth. High cooling rates and its short residence times help in the Nanoparticle formation. In contrast to wet phase synthesis, we can achieve higher production rates for Gas-phase synthesis.[17]

1.2.5 Mesoporous-mediated synthesis

Before the synthesis of mesoporous materials, the inorganic precursor is synthesized. The inorganic precursor is mixed with non-ionic surfactant followed by hydrothermal treatment. Mesoporous materials are impregnated with the perovskite precursor solutions, and after air-drying, they form perovskite-mesoporous material nanocomposite at room temperature and ambient atmosphere. The surfactant and inorganic framework sources are combined through

cooperative nucleation. Finally, separation and drying need to be done to remove the surfactants. Mesoporous materials are having enormous pores smaller than 2nm.[18,19]

1.3 Lead-free halide perovskites

In recent years, the development of lead-free halide perovskite has significantly increased their applications in optoelectronic and photovoltaic technologies because of obtaining advantages over long-term moisture and thermal stability problems and the absence of toxic metal.[20] Lead-free halide perovskites gain popularity because of their intrinsic properties, such that narrow-band emission, wide wavelength tunability, and long carrier diffusion lengths. In the lead-based halide perovskites, a toxic heavy metal, Pb itself, is a significant barrier to large-scale commercialization.[21, 22] Perovskite materials containing nontoxic metals such as Silicon, tin, and Germanium used to replace toxic metal Lead have been studied. It was recently reported that nanosized lead-free Cesium tin halide perovskite could also be synthesized.[23] However, some of the Pb substitutions are ineffective because they readily oxidize and degrade the perovskites materials. It also destroys both the ns^2 configuration and 3D perovskite structure that we got in Pb-based perovskites.[24]

The next choice is to replace the Pb with trivalent cations like Bi and Sb to remove the toxicity and showing lower toxicity and stable ns^2 configuration compared to lead-based perovskites. However, substituting a trivalent M(III) cation for bivalent Pb (II) cation creates charge imbalance in the $AM(III)X_3$ (or $A_3M_3(III)X_9$) perovskite structure, converting it to $A_3M_2(III)X_9$ (or $A_3M_2(III)X_9$, where is an ordered M(III) vacancy site.[25-28] As a result, the bandgap and effective masses of charge carriers develop. Furthermore, $A_3M_2(III)X_9$ layered perovskites' defect tolerance behaviour is dubious. Overall, Layered perovskites $A_3M_2(III)X_9$ are fascinating and are currently being studied, as shown in figure 2. However, their optoelectronic characteristics are substantially relatively low to those of $APbX_3$ Perovskites at the moment.[29]

The generic formula for metal halide double perovskites is $A_2M'(I)M(III)X_6$ (A: Cs, CH_3NH_3 (Monovalent cation); M′(I): Cu, Ag, Au, In, K; M(III): Bi, Sb, In (Trivalent cation); X: Cl, Br, I (halogen) are currently being investigated to preserve charge neutrality as well as the 3D perovskite structure. These metal halide Double Perovskites (DPs) have a structural resemblance to well-researched oxide DPs with the general formula $A_2B'B''O_6$. $Cs_2AgBiCl_6$

and $Cs_2AgBiBr_6$ were some of the first halides DPs investigated. However, due to their wide (>2 eV) and indirect band gaps, they are not effective solar light absorbers.[30,31] Alloying trivalent metal cations have tuned $Cs_2AgBiBr_6$'s bandgap (In, Sb, and Tl) with Bi and applying high pressure, but the band gap's indirect nature preserved.[32-34] There are several other double perovskites (DPs) materials with wide direct band gaps, such as $(CH_3NH_3)_2KBiCl_6$, $Cs_2AgInCl_6$, $(CH_3NH_3)_2KGdCl_6$, and $(CH_3NH_3)_2KYCl_6$, and indirect band gaps, such as $Cs_2AgSbCl_6$, $(CH_3NH_3)_2AgBiBr_6$, $(CH_3NH_3)_2AgSbI_6$, were identified shortly after these two materials. Some Indium-based DPs were identified, such as $Cs_2InSbCl_6$ and $Cs_2InBiCl_6$. Because of oxidation to In, indium-based DPs are thermodynamically unstable (III). The band gaps of different DPs have been empirically and analytically researched.

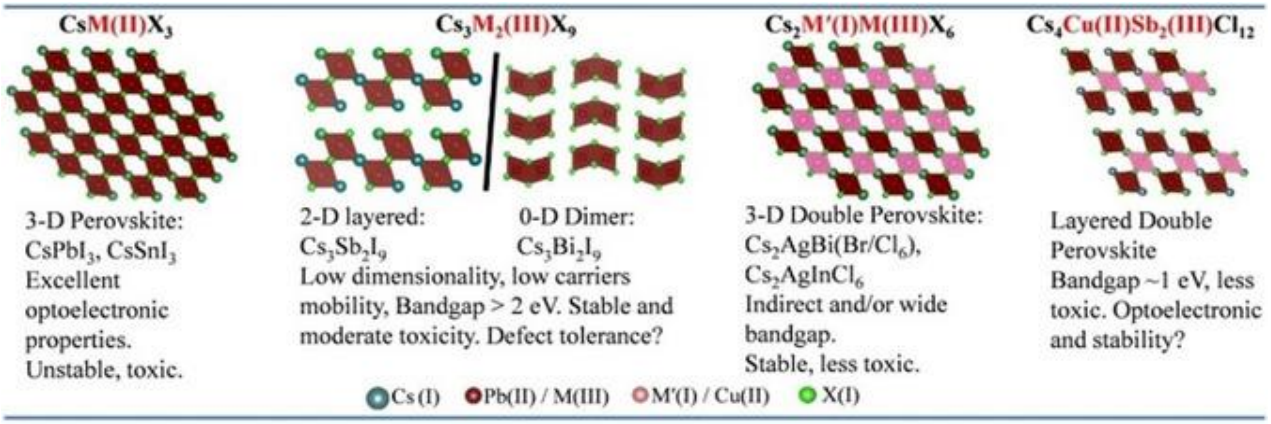

Figure 2. Different reported structures of metal halide perovskites (copyright permission from Ref. 14)

1.4 Lead halide perovskites

In recent years, lead halide perovskites have got a lot of coverage for their vibrant application due to their high retaining power, scalability, defect tolerance, tunable bandgap, and simple single crystal growth from low-cost solution processes.[35] Organic-inorganic lead halide perovskites have recently been considered as leading photovoltaic materials. At the same time, more than 20% of energy conversion efficiency has since been certified. A deeper understanding of the material properties contributing to these notable performances could allow for even higher efficiency.[36] Photodetectors are all examples of light-emitting diodes

(LEDs).[37] It exhibits high photoluminescence (PL) and a wide bandgap, as well as long-range charge transport and high absorption coefficients.[38]

Two main reasons to ensure the performance of Pb-based perovskites are their $6s^2$ electronic configuration, which is the primary cause of the antibonding condition at the valance band limit (VBM), and the 3D network via corner shared $[PbI_6]^{4-}$octahedra.

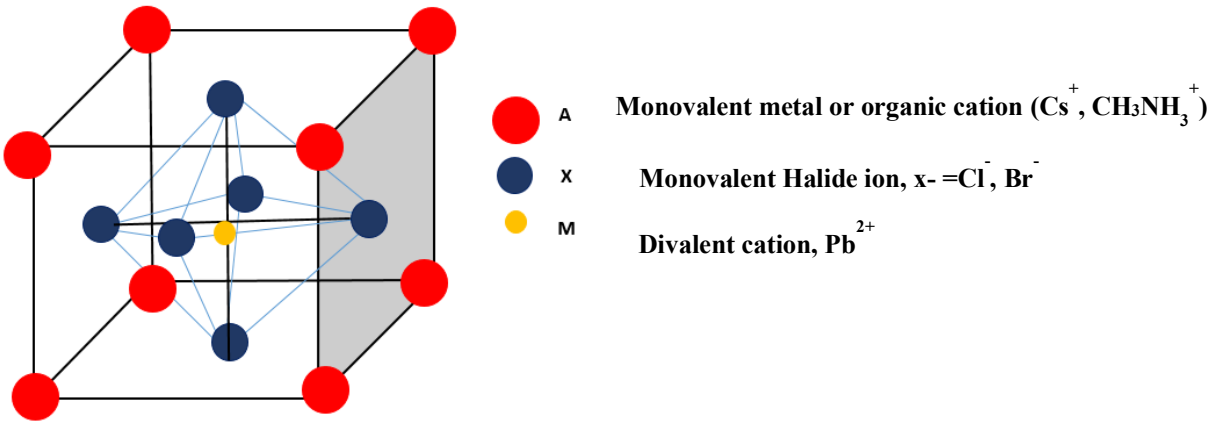

Figure 3. The cubic crystal structure of 3D Lead halide perovskite(figure reproduced from Ref. 37)

1.4.1 Ruddlesden–Popper 2D Lead Halide Perovskite

Ruddlesden–Popper perovskites have attracted a lot of attention as potential candidates for optoelectronic devices. Organometallic halide perovskites in 2D and corrugated 2D are generated by severing 3D perovskites, known as Ruddlesden–Popper perovskites (RPPs), along lattice orientations 001 and 110. (figure 4(b,c)).[37] They are having general formula $(A')_2(A)_{n+1}B_nX_{3n+1}$. Wherein A′ represents RNH_3 or H_3NRNH_3 (R aromatic or aliphatic organic ligands) and serves as an insulating surface between the various inorganic layers made up of metal halide octahedral units that corner atoms share. Cs^+ and $CH_3NH_3^+$ are examples of small cations represented by A, B denote a divalent metal cation (Pb^{2+} or Sn^{2+}), and X indicates halides. [38] In the last ten years, the use of organic-inorganic hybrid lead iodide perovskites as light absorption materials increased the power conversion efficiency (PCE) of solar cells from 3.8 % to 24.2 %.[39] The tolerance factor, 't' for stable 3D perovskite structures should be in the

range of 0.8 to 1. Corner sharing halide anions connect the metal halide $[BX_6]^{4-}$ octahedral units structurally, and the A cations fill voids in the structure, as shown in figure (3).[40] As large organic cations replaced A, they did not fit in the voids between the $[BX_6]^{4-}$ octahedra, forcing the network to form a 2D structure.

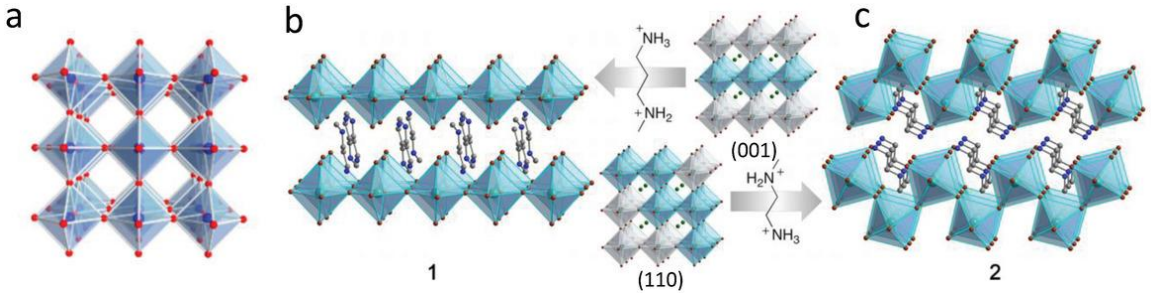

Figure 4. Crystal structures of **(a)** 3D perovskite**, (b)** (001) 2D perovskite (N-MPDA) $[PbBr_4]$, and **(c)** (110) 2D perovskite (copyright from Ref. 37)

The symbol 'n' represents the number of metal halide monolayer sheets sandwiched between the insulating A organic layers, n = 1, pure 2D structure, n = 2–5, quasi2D structure, n =∞, 3D structure.[41]

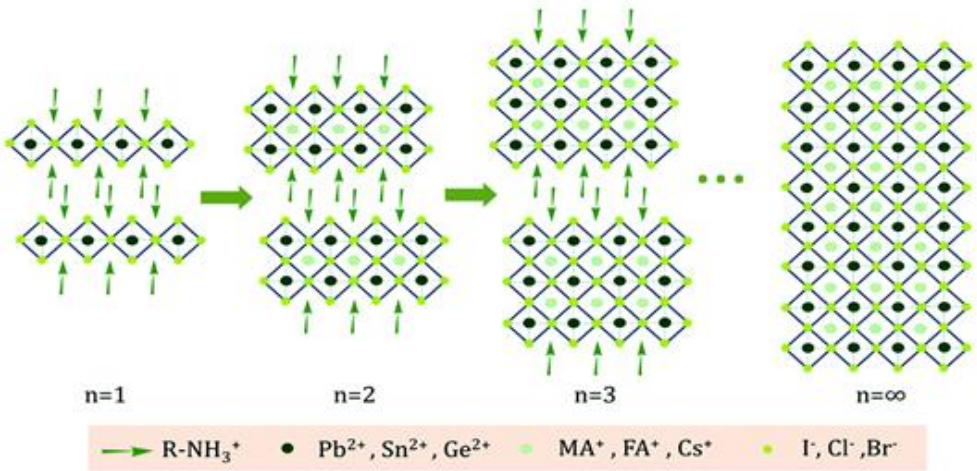

Figure 5. Schematic layered organic-inorganic halide perovskites. R is an organic group, sheets (copyright permission from Ref. 43)

Reported 2D organic-inorganic Lead hybrid halide perovskites based on two key components: inorganic layers and their modulation and organic cation variety.[42] 2D halide perovskites are very efficient compared to 3D halide perovskites in optoelectronic devices due

to their strong quantum confinement effect, high exciton binding energy, and superior moisture stability. By changing the organic ligands, and inorganic layers, the optical properties and crystal structure of 2D perovskite materials can also be changed, allowing for bandgap tuning and a broad emission wavelength. Furthermore, these organic ligands directly influence the electronic properties of the inorganic substrate by twisting the soft inorganic structure.[43]

1.5 Usage of perovskites as a photocatalyst

There has been widespread concern over many environmental severe issues that we face globally in recent years. One of them is about water, our most valuable natural resource. An increasing population combined with rapid industrial growth has resulted in a steady rise in water contamination in many areas of the world due to the increased release of harmful agents. As the need for clean water increases, the demand for new purification technologies with low environmental impact grows.[44] Recognizing these needs and developing efficient, sustainable, and environmentally friendly water treatment technologies is crucial for our future. Heterogeneous photocatalysis has emerged as an advanced and promising technology for wastewater treatment. Photocatalysis is a process in which highly reactive short-lived species are formed in a photocatalyst material under exposure to light energies higher than or equal to the photocatalyst bandgap. These reactive species' high oxidizing activity will cause degradation and, eventually, complete mineralization of many refractory organic and inorganic contaminants in water.

$$\boldsymbol{h\nu \geq E_g}$$

Contaminants + Photocatalyst $\longrightarrow$ CO_2+ H_2O+ Intermediates

Different applications of photocatalysis.

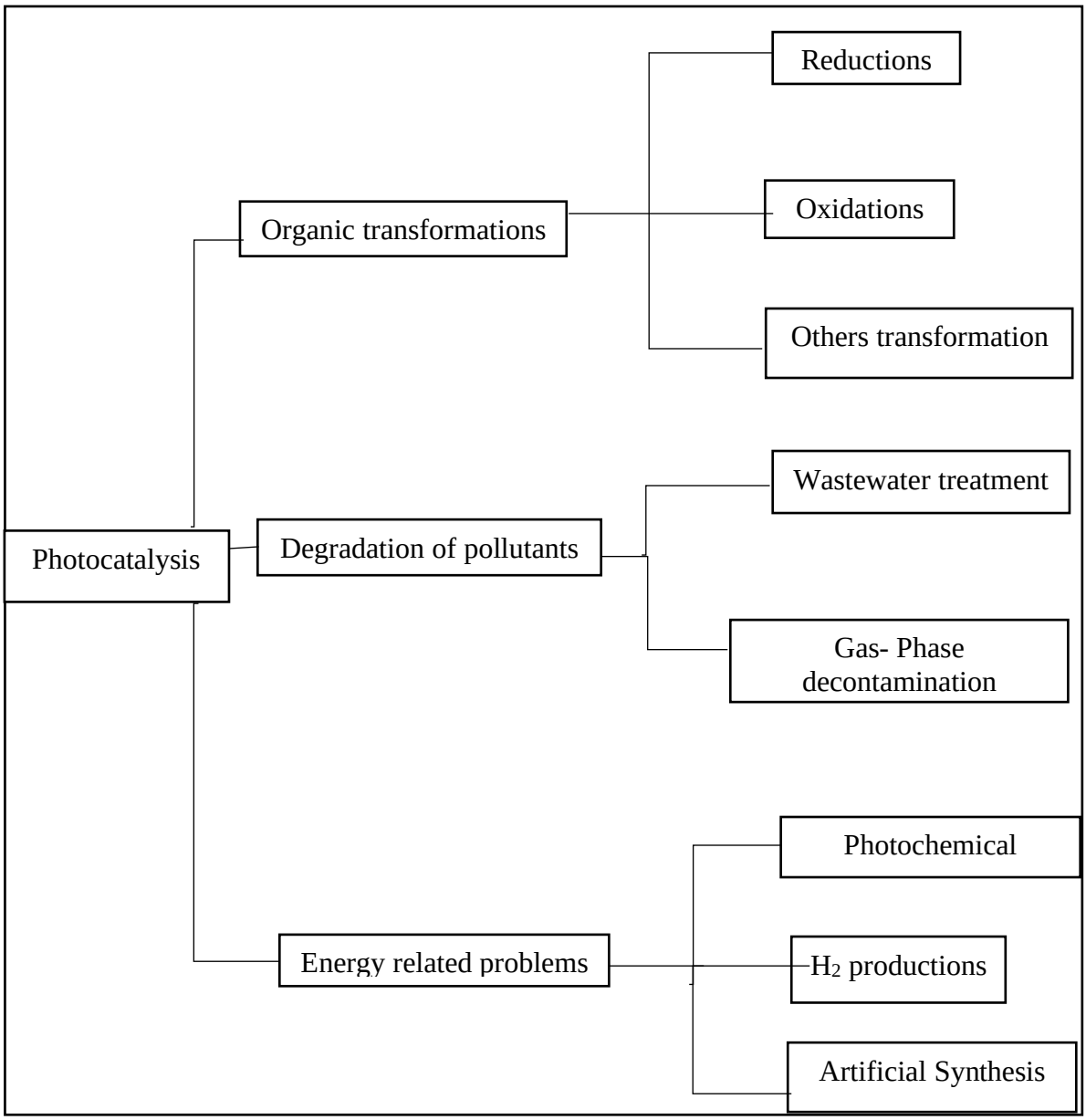

1.5.1 Principles of heterogeneous photocatalysis

When a given semiconducting photocatalyst is irradiated with a photon of energy equal to or higher than its bandgap, an electron jumps from its valence band to its conduction band within significantly less time.[45,46] The electrons and holes generated are in the CB and VB, respectively, separated by the bandgap. The fate of the isolated electron and hole will take various paths. One possibility is that photogenerated electrons and holes will recombine in bulk or on the semiconductor's surface, releasing energy in the form of heat or photons. The recombination quenches the photocatalytic activity of the semiconductor photocatalyst. Another possibility is electrons and holes that migrate to the semiconductor's surface without recombination will reduce and oxidize the reactants adsorbed by the semiconductor photocatalyst, respectively. As shown in figure 6 below, at the surface, the photocatalyst can donate the electron to an electron acceptor (**A**), usually molecular oxygen. In turn, a donor species (**D**) can be oxidized by the valence band hole.[47] These charge transfer processes depend on the valence band, the conduction band edges, respectively, and the adsorbed species' redox potential. The primary photocatalytic hydrogen production and photocatalytic water/air purification are reduction and oxidation reactions of environmental contaminants. Nanosized semiconductors can improve both surface adsorption and photocatalytic reactions by providing more photocatalytic active surface area.[48]

The primary photocatalytic events have given by reactions below

$$\textbf{Semiconductor} \xrightarrow{h\nu \geq E_g} e^-_{CB} + h^+_{VB}$$

$$h^+_{VB} + \mathbf{D} \longrightarrow \mathbf{D}^{\cdot +}$$

$$e^-_{CB} + \mathbf{A} \longrightarrow \mathbf{A}^{\cdot -}$$

$$e^-_{CB} + h^+_{VB} \longrightarrow \Delta \textit{ and/ or } h\nu$$

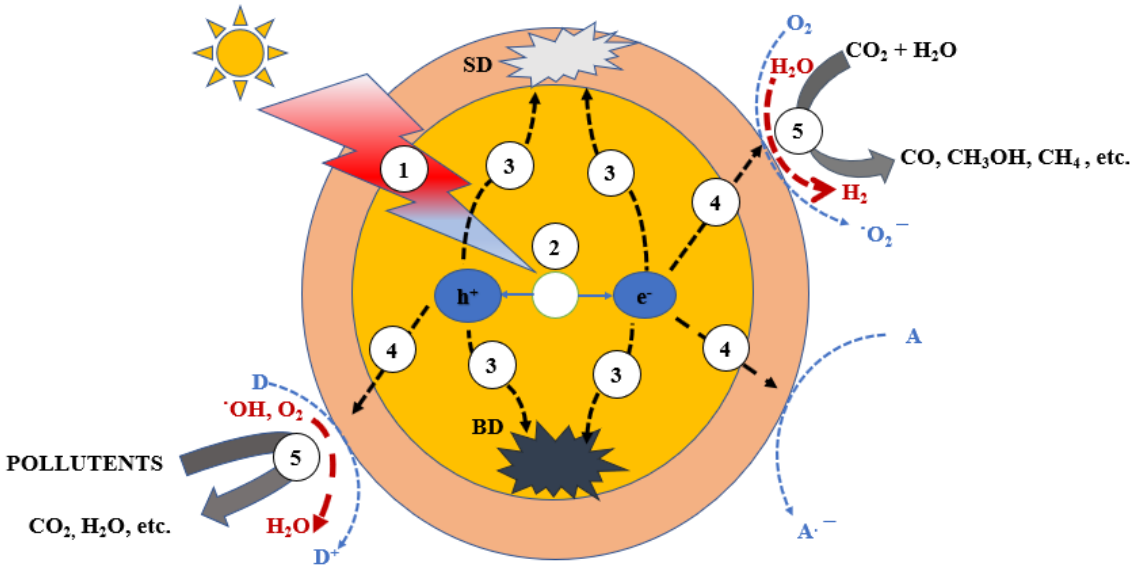

Figure 6. Schematic of the main processes in a photocatalytic reaction (figure reproduced from Ref. 49)

- BD Bulk Defects
- SD Surface Defects

1. Photon exciton
2. Charge Separation
3. Charge Recombination
4. Charge Transfer
5. Redox Reactions

1.5.2 Mechanisms of the Photocatalytic Process for wastewater treatment

The photocatalytic process initiated with the absorption of a photon (hυ)

$$\textbf{Semiconductor} \longrightarrow e^{-}_{CB} + h^{+}_{VB}$$

When an aqueous photocatalytic material is exposed to light with an energy greater than its bandgap energy, the photogenerated electrons could reduce the dye or react with electron acceptors like O_2 adsorbed on the surface of the photocatalytic material or dissolved in water, reducing it to superoxide radical anion $\cdot O_2^-$. The photogenerated holes may either oxidize the organic molecule to form R^+ or react with **OH** or H_2O to form $\cdot OH$ (hydroxyl radicals). They are stated to be responsible, along with other high oxidant species (peroxide radicals), for the heterogeneous TiO_2 photodecomposition of organic substrates as dyes.[49] According to this, the related reactions at the semiconductor surface that cause dye degradation are as follows, as shown in figure 7.[50]

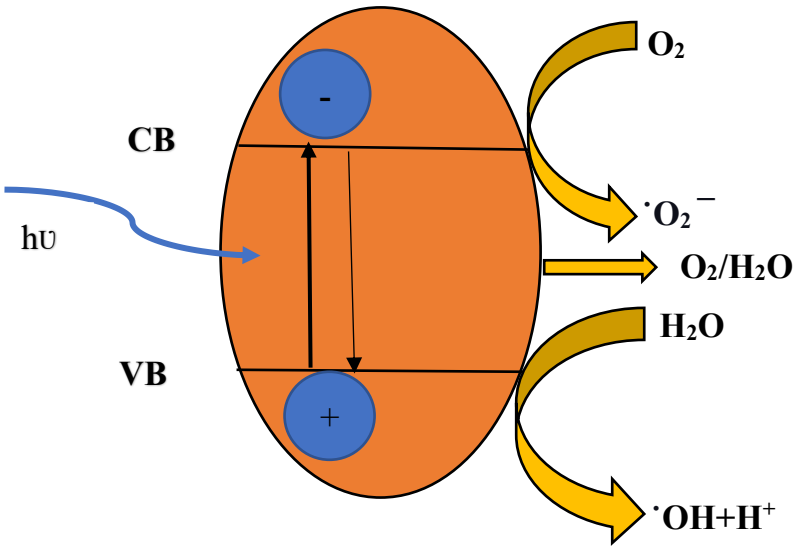

Figure 7. Schematic diagram of Band structure

Different reactions involving conduction band

$$e^-_{CB} + O_2 \longrightarrow \cdot O_2^-$$

$$e^-_{CB} + \cdot O_2^- + 2H^+ \longrightarrow H_2O_2$$

$$e^-_{CB} + H_2O_2 \longrightarrow \cdot OH + OH^-$$

$$\cdot O_2^- + H_2O_2 \longrightarrow \cdot OH + OH^- + O_2$$

$$^{\bullet}O_2^{-} + H^{+} \longrightarrow {}^{\bullet}HO_2$$

$$(e^{-}_{CB}) + {}^{\bullet}HO_2 \longrightarrow HO_2^{-}$$

$$HO_2^{-} + H^{+} \longrightarrow H_2O_2$$

$$2\ {}^{\bullet}HO_2 \longrightarrow O_2 + H_2O_2$$

Reactions involving valence band h^{+}

$$h^{+}_{VB} + H_2O_{ads} \longrightarrow {}^{\bullet}OH_{ads} + H^{+}$$

$$h^{+}_{VB} + 2H_2O_{ads} \longrightarrow 2H^{+} + H_2O_2$$

$$h^{+}_{VB} + OH^{-}_{ads} \longrightarrow {}^{\bullet}OH_{ads}$$

$$\text{Dye} + {}^{\bullet}OH_{ads} \longrightarrow \text{Degradation products}$$

A photocatalyst is distinguished by its ability to simultaneously adsorb two reactants that can be reduced and oxidized by efficiently absorbing light ($h\nu \geq E_g$). According to thermodynamics, the adsorbate's redox potential (acceptor) should be lower than the semiconductor's conduction band. If the adsorbate is the donor, its potential level should be higher than the semiconductor's valence band position to donate an electron to the empty hole in the valence band. The reduction mechanism refers to the process of transferring an electron from the semiconductor to the adsorbate. In contrast, the oxidation mechanism refers to moving an electron from the adsorbate to the semiconductor. Figure 7 depicts these processes. Thus, the energy level at the bottom of the conduction band determines photoelectrons reduction potential, while the energy level at the top of the valence band determines holes oxidizing ability. If the adsorbed couples are water and dissolved oxygen (H_2O/O_2), water is oxidized by positive holes and splits into $^{\bullet}OH$ and H^{+}. Since oxygen is easily reducible, the conduction band's photoelectron produces superoxide radical anions ($^{\bullet}O_2^{-}$), which react with H^{+} to produce hydrogen dioxide radical (HO_2, hydroperoxyl). Following collisions with an electron to form a hydrogen dioxide anion (HO_2^{-}), hydrogen peroxide anion, and then hydrogen ion, a

molecule of H_2O_2 is formed.[50] The resulting hydroxyl radical (•OH), a potent oxidizing agent (standard redox potential +2.8 V), will oxidize most of the dye.

Detection of •OH (hydroxyl radicals)

Previous studies on various photocatalytic reactions led to the hypothesis that •OH radicals generated by oxidation of surface hydroxyl or adsorbed water play an important role in initiating oxidation reactions.[51, 52] •OH, (hydroxyl radicals) formed by the oxidation of either water or adsorbed hydroxide ions with photogenerated holes. Spin trapping with Electron Paramagnetic Resonance spectroscopy (EPR) revealed •OH (hydroxyl radicals)' existence on the irradiated photocatalyst's surface.[53, 54] Nakato and colleagues and others have discovered flaws in this simple electrochemical method.[55, 56] They proposed an alternative pathway in which •OH (hydroxyl radicals) produced by a nucleophilic attack of water on a hole trapped at the surface lattice oxygen.[57] TiO_2 is currently the most effective and commonly used catalyst in photocatalytic reactions. Other semiconductors widely used as catalysts include ZnO, ZnS, CdS, Fe_2O_3, and SnO_2.[58]

1.5.3 Role of different scavengers in heterogeneous photocatalysis

Further studies include understanding the mechanism and confirming the photocatalyst activity through various photocatalytic reactions. As already discussed, the primary active species involved in a photocatalytic process are the VB holes, CB electrons, hydroxide radicals (•OH), and superoxide radicals ($•O_2^-$). It is necessary to identify which active species are mainly involved in the photocatalytic reaction. Researchers used various scavengers to determine the mechanism of different photodegradation reactions of dye. We can vary the kinetics of different heterogeneous photocatalysis reactions using suitable scavengers. There have been numerous reported scavengers that can either enhance or inhibit photocatalytic activity.

The effect of electron and hole scavengers studied on photocatalytic degradation of organic matter in the presence of suspended TiO_2 particles. The method used to find a trace of heavy metal Cd (II) in water by the recovery of voltammetric wave in the presence of EDTA, chosen as a ligand that behaves like dissolved organic contaminants. The accelerating power of O_2 was verified as an electron scavenger. It was analyzed in the absence of O_2 by providing an anaerobic condition, but here nitrate ion works as an electron scavenger. So in the case of the

aerobic state, O_2 works like an electron scavenger where they scavenged the electron and stopped the electron- holes recombination. Further providing more electron and holes that helps in degradation and reduction-oxidation of complex contaminants. Additionally, the above reaction proceeded in the presence of hole scavengers like ethanol and methanol, which also stopped electron-holes recombination.[59]

To assess oxidative organisms' existence and significance, organic and inorganic substances are used as scavengers and are supposed to react fast and precisely with a radical, generating a stable species that does not interfere with the reaction, thereby eliminating the effect of this radical in the degradation. Many molecules are used as radical scavengers in heterogeneous photocatalysis; for instance, to scavenge the hole in the valence band, electron donor species such as oxalate and formic acid are employed respectively. The effect of these scavenger singnificantally helps in varying the photocatalytic reaction kinetics. Alcohols, such as *t*-butanol and methanol, are usually applied to confirm the contribution of $^{\cdot}OH$; *para*-Benzoquinone extensively used to attest the presence of superoxide ion radicals/hydroperoxyl radicals ($^{\cdot}O_2^{-}/HO_2^{\cdot}$).[60]

The photocatalytic dye degradation reaction of Rhodamine B(RhB) and methyl orange (MO) dye performed using $ZnIn_2S_4$ as photocatalyst under visible light. It was observed that Superoxide radicals were the key species, and hydroxyl radicals played a supplementary role during the photocatalytic process. The addition of hole scavengers to inhibit the recombination of holes and electrons in the reaction medium improved the photocatalytic degradation of MO dye because more electrons reduce oxygen to superoxide radicals.[61]

The photocatalytic degradation reaction of MB (methylene blue) was carried out using a developed $BiVO_4$ photocatalyst. The active species such as $^{\bullet}O_2^{-}$ and $^{\bullet}OH$ radicals generated will react with dyes, resulting in degradation of dyes concentration in the system. However, the fast recombination rate between electron-hole pairs has been a limiting factor that hindered this photocatalytic degradation system's effectiveness. The addition of $AgNO_3$ as an electron scavenger yielding 100% photocatalytic degradation of methylene blue in 120 minutes under visible-light irradiation.[62]

1.6 Current Work

Lead-free perovskites come up to remove significant lead hurdles toxicity and their scalability and widespread commercialization. As a result, lead-free perovskites are regarded as a boon to the future of photovoltaic technology to meet the real need for electricity. In this regard, we present a detailed review of lead-free perovskite nanocrystals that allowed the replacement of lead metal by hetero-valent metal substitutes. Since there are few reports on the synthesis of $Cs_4CuSb_2Cl_{12}$, most of them are in the micron size range, except a top-down synthetic protocol that yields the material in the nano-size range. This work describes a bottom-up synthesis for producing direct bandgap monodisperse $Cs_4CuSb_2Cl_{12}$ nanocrystals using the hot injection synthesis method. This work aims to synthesize 2D layered $Cs_4CuSb_2Cl_{12}$ perovskite nanocrystals followed by characterization via different techniques while also monitoring its photocatalytic activity in heterogeneous Catalysis as it shows a lower bandgap.

Lead halide perovskites received a lot of attention due to various applications ranging from photovoltaic solar cells to photocatalysis. Different research groups have tried to use these materials for white light-emitting devices. Tunability of emission wavelength is possible by mixed halide composition, but the effects of these hybrid halide components are compromised due to anion exchange. This work aims to synthesize the Ruddlesden popper 2D perovskites $(BA)_2PbCl_4$ and dope them with the help of Cu^+ and Cu^{2+} metal ions. We used Various characterization techniques to analyze the synthesized perovskites to understand the change in the bandgap, optical, and structural properties due to this doping on the $(BA)_2PbCl_4$,[63,64] tracking its photocatalytic activity, including heterogeneous catalysis.

1.7 Instrumentation

The UV-visible spectra of the NCs distributed in toluene were measured using a Cary 5000 UV-Vis NIR spectrophotometer (Agilent Technologies) at a scan rate of 1 nm/s from 280 to 1100 nm. Powder X-Ray Diffraction (PXRD) data were collected using a Rigaku Ultima IV diffractometer outfitted with Cu K (1.54) radiation and a scan rate of 2°/min ranging from 15 to 60°. JEM-F200 (JEOL) transmission electron microscopic (TEM) studies were performed with an energy dispersive X-ray scattering (EDX) facility. The JEOL-7600F was used for FESEM (field emission scanning electron microscopy). TGA analysis was carried out on a Shimadzu DTG-60H with a heating rate of 5 °C/min up to 1000 °C. Perkin Elmer DSC 8000 was used for DSC research. During research, ultraviolet photoelectron spectroscopy (UPS) was used to calculate the work function. Thermofisher scientific's Nexsa model was used for X-ray photoelectron spectroscopy (XPS). Electron paramagnetic resonance (EPR) spectra were collected using a Bruker MicroX spectrometer in X-band frequency (microwave frequency, 9.44 GHz) at room temperature, and measurements were carried out with scratched-off films. Perkin Elmer was used to analyzing the FTIR characteristics from 400–4000 cm^{-1}.

Chapter 2

Project 1. Synthesis of 2D layered $Cs_4CuSb_2Cl_{12}$ double perovskite and its photocatalytic activity

Experimental section

2.1 Materials

Cesium carbonate (Cs_2CO_3,Sigma Aldrich, 99.995%), lead (II) chloride ($PbCl_2$, Alfa Aesar, 99%), manganese chloride tetrahydrate ($MnC_{l2}.4H_2O$,Merck,99%), Oleyl amine (OAm, Sigma Aldrich, 70%), oleic acid (OA, Sigma Aldrich, 90%), 1-octadecene (ODE, Sigma Aldrich, 90%), Trioctyl phosphine(TOP, Sigma Aldrich), Acetone (Rankem, 99%), Dichloromethane (DCM,Rankem,99%) , Methoxy ethanol(Loba Chemie, 99%), Methoxy acetic acid (Alfa Aesar, 97%) and branched polyethyleneimine PEI (MWt = 1800) (Alfa Aesar 99%), Methanol (Fischer Scientific, 99%). Antimony (III) acetate ($Sb(ac)_3$, Sigma Aldrich, 99%), Diphenyl Ether (DPE, Spectrochem) and Benzoyl Chloride (Bz-Cl, Fischer Scientific), trimethylsilyl chloride (TMSCl, >99%, Sigma-Aldrich), hydrochloric acid (HCl, 37%, Merck), hydrobromic acid (HBr, 47%, AVRA), Congo red (Sigma-Aldrich), potassium ferricyanide($K_3Fe(CN)_6$, Fisher Scientific), *t*-butyl alcohol (Sigma-Aldrich), coumarin (Sigma-Aldrich), and ammonium oxalate monohydrate ($(NH_4)_2C_2O_4.H_2O$, Sigma-Aldrich), Antimony Trichloride ($SbCl_3$, SRL, 99%), Copper (I) chloride (CuCl, Sigma Aldrich, >90%), Silver Chloride (AgCl, Sigma Aldrich, 99%), Cesium Chloride (CsCl, Sigma Aldrich, 99.9%)

2.2 Synthetic Protocol of $Cs_4CuSb_2Cl_{12}$ double perovskite

2.2.1 Synthesis of 2D layered $Cs_4CuSb_2Cl_{12}$ NCs via hot injection method

The synthesizing protocol for NCs slightly changed from Manna et al.1. Before the synthesis of $Cs_4CuSb_2Cl_{12}$ in a Schlenk flask, to make the Cs-oleate precursor, 400 mg of Cs_2CO_3 was mixed with 16 ml DPE and 2.4 ml of OA. This mixture was vacuum dried for 1 hour at 120°C with vigorous stirring before being heated to 150°C in a nitrogen atmosphere. The transparent Cs-oleate solution preserved for later use.[65]

In a 50 mL Schlenk flask, 0.25 mmol of $CuCl_2.2H_2O$ and 0.25 mmol of $Sb(ac)_3$ were dissolved in the mixture of DPE (1ml), dried OA (1ml), dried Cs-oleate and OAm (1ml) to synthesize $Cs_4CuSb_2Cl_{12}$ NCs (DPCl1). The reaction mixture was vigorously stirred under a vacuum at 120°C for 1 hour to extract the moisture. The slank flask removed from the vacuum, and the N_2 nitrogen gas flow began to create an inert atmosphere, gradually raising the temperature to 150°C.

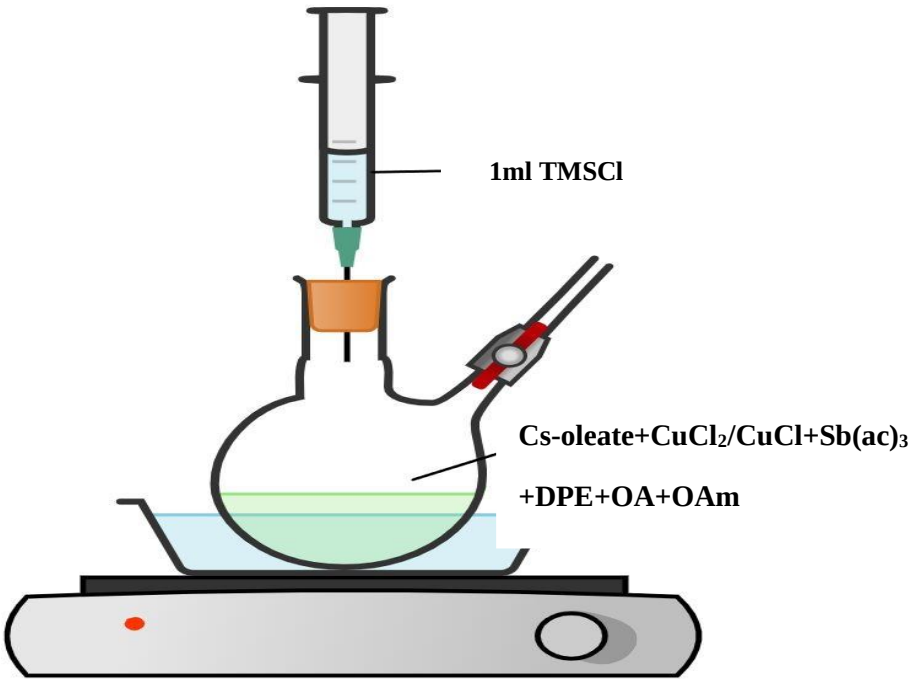

Figure 8. Hot injection synthesis of 2D Layered $Cs_4CuSb_2Cl_{12}$ NCs

After the reaction temperature reached 150 °C, 1 mL of TMSCl mixture was quickly injected into the reaction mixture and transferred to an ice bath after 10 seconds to quench the reaction. The resulting solution was brownish in colour. It was washed twice with toluene and centrifuged at 8000 rpm for 20 minutes. DPCl1 is the name given to the obtained nanocrystals.[66]

2.2.2 Synthesis of 2D $Cs_4CuSb_2Cl_{12}$ NCs via acid-mediated solution-phase method

In this process, 1 mmol $CuCl_2$ and 1 mmol $SbCl_3$ were mixed in 5 mL of 37 % concentrated HCl solution. After 30 minutes of proper stirring, the reaction mixture was heated to 75°C, and 2 mmol of CsCl was added, which was retained for 1 hour with continuous stirring. A black precipitate formed and was washed with ethanol before being filtered out and yield black powdered $Cs_4CuSb_2Cl_{12}$ MCs (DPCl2).[67] The same technique was used to synthesize $Cs_4CuSb_2Br_{12}$ (DPBr2) using $SbBr_3$, CuBr, and CsBr as precursors in a concentrated HBr (47%) solution.

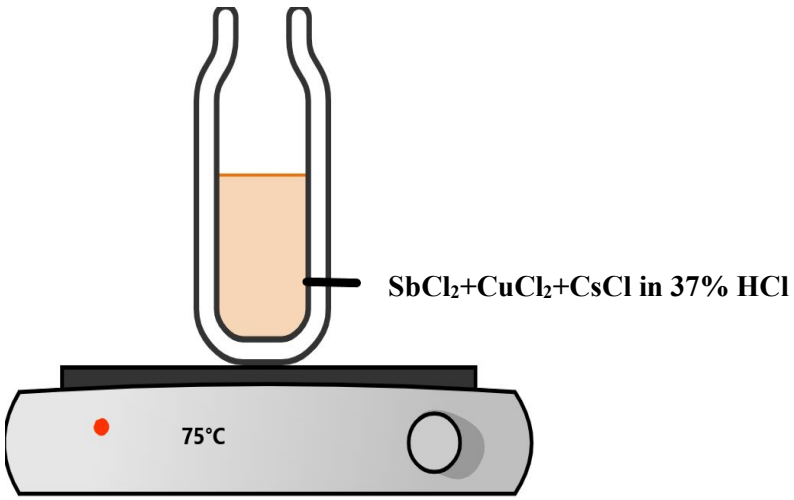

Figure 9. Acid-mediated solution-phase synthesis 2D Layered $Cs_4CuSb_2Cl_{12}$ MCs

2.3 Results and Discussion

TEM, PXRD, and AFM studies were used to analyze the chemical and structural properties of the $Cs_4CuSb_2Cl_{12}$ NCs obtained by hot injection, and TGA and DSC were used to analyze the thermal properties. PXRD and FESEM were performed on $Cs_4CuSb_2Cl_{12}$ MCs. These findings indicate that the synthesized perovskite is highly stable under a variety of conditions. Its bandgap and particle morphology demonstrates that it is highly effective for sunlight-driven applications.[66]

The FESEM study reveals the formation of octahedral microcrystals. TEM-EDX analysis was used to investigate the structural morphology and composition of $Cs_4CuSb_2Cl_{12}$ NCs. The particle shape was found to be spherical with a scale of 3.9 nm on average. Elemental mapping corresponding to each element in the sample indicating the Cu and Sb are abundant in the selected area. The ideal temperature for the reaction is 150°C because when the reactions are carried out at 180^0C, the product gets agglomerated. XPS data verified the development of $Cs_4CuSb_2Cl_{12}$ NCs with the respective oxidation states of the constituent elements (Cs, Cu, Sb, and Cl) present in NCs. The thermal properties of the NCs were studied using TGA and DSC. The sample was found to be stable up to 185°C and after that started losing the weight till 725°C. Weight loss can be ascribed to the evaporation of organic solvents and ligands at low temperatures and the inorganic part's evaporation at higher temperatures. The sample was heated from -10°C to 210°C and then cooled down to -10°C without any phase transition from ambient (room) temperature to 180°C. AFM study was used to determine the topography and height of the NCs. The microscope's cantilever was screened over the sample's surface, revealing disc-shaped nanocrystals of an average thickness of 1nm, corresponding to a single unit cell's length.[66]

Powder XRD was used to examine the crystal structure of the synthesized NCs. The obtained $Cs_4CuSb_2Cl_{12}$ NCs (DPCl1) were found to be phase pure and fit well with the previously mentioned 2D layered $Cs_4CuSb_2Cl_{12}$ MCs (figure 10).

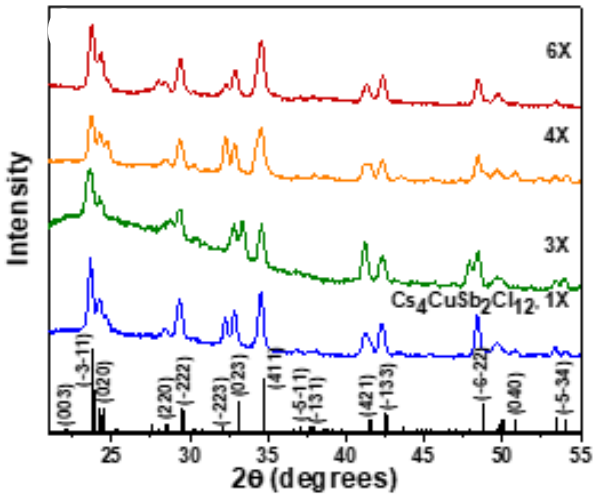

Figure 10. Compares the XRD patterns of synthesized $Cs_4CuSb_2Cl_{12}$ NCs to the JCPDS results at different scaled-up batches[66]

Figure 11 depicts the absorption spectrum of $Cs_4CuSb_2Cl_{12}$ nanocrystals distributed in toluene. The nanocrystals have a broad absorption peak at 556 nm, and the corresponding Tauc plot reveals a narrow bandgap of 1.3 to 1.6 eV. The bandgap here appears to be very promising for sunlight-driven reactions.

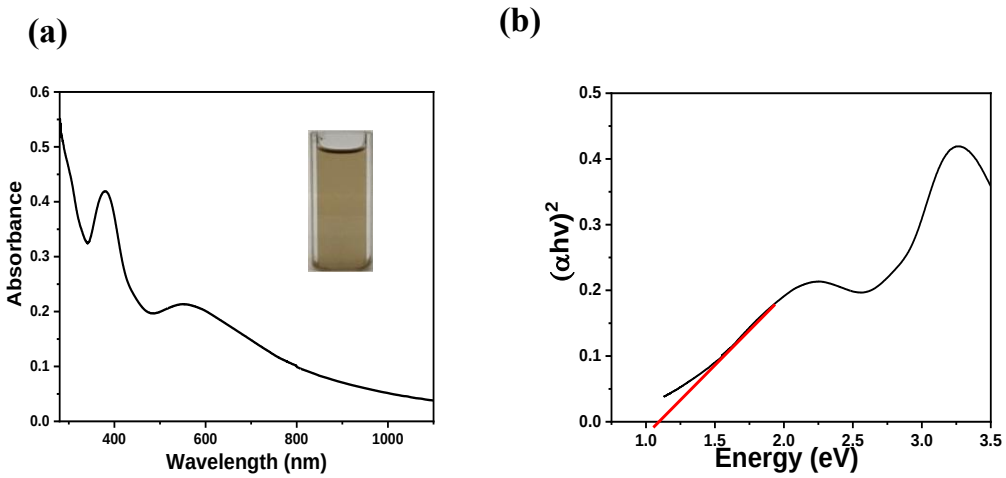

Figure 11. (a)UV-Vis spectrum and **(b)** Tauc plot of $Cs_4CuSb_2Cl_{12}$ NCs[66]

The valence band maximum (VBM) position is calculated by ultraviolet photoelectron spectroscopy (UPS), which, when combined with the bandgap value obtained, yields the conduction band minimum position, (figure 12 (a,b,c)).

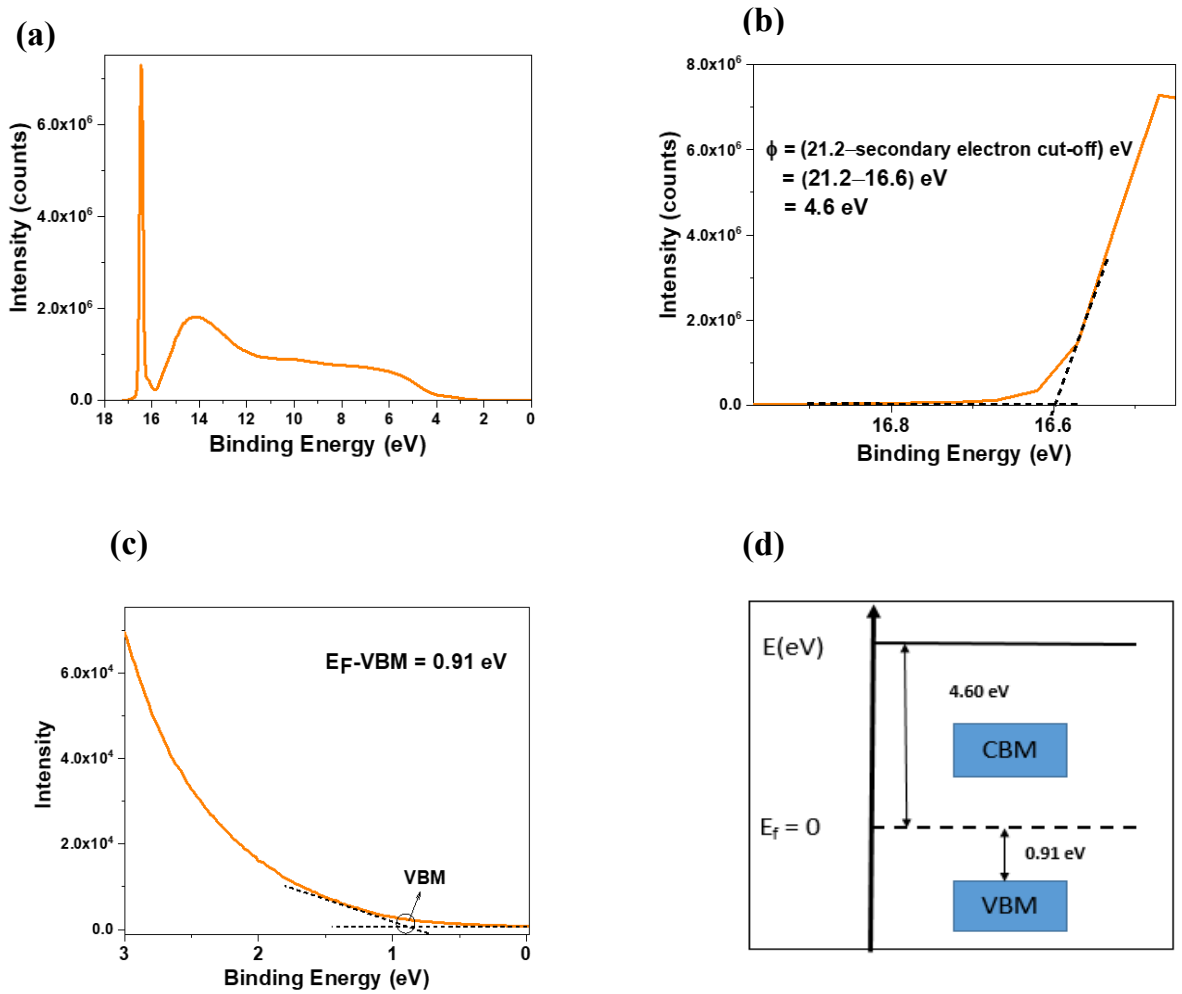

Figure 12. (a)-(c) He1 UP spectral scan of DPCl1 **(d)** Schematic diagram of Band structure of DPCl1

The Valence band maximum (VBM) location is approximately 0.91 eV lower than the Fermi stage. Figure 12. (d) depicts a graphical representation of the band structure with an optical band gap of 1.57 eV.

The existence of Cu^{2+} is also indicated by DPCl1 Nanocrystals' X-band electron paramagnetic resonance (EPR) spectrum at room temperature, displaying a signal with a center frequency of 3187 Gauss leads to Cu^{2+} (figure 13). The reason behind it is an unpaired electron in the Cu^{2+}, d^9 system, with the total electron spin S = 1/2 and nuclear spin of I = 3/2, but no hyperfine splitting was observed, as previously mentioned, suggesting spin in Cu (II) centers couples with one another.[14]

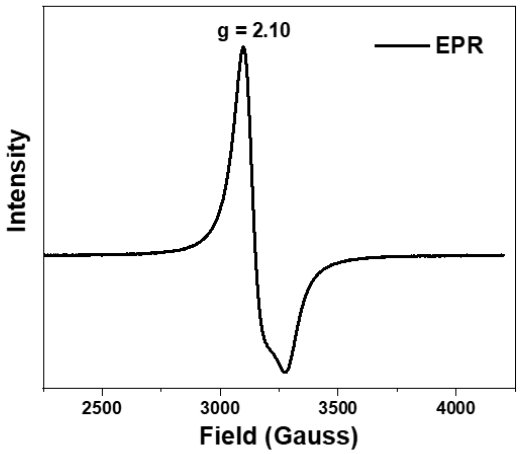

Figure 13. X-band EPR spectra for Cu^{2+} in DPCl1 NCs at room temperature

.

2.4 Application of $Cs_4CuSb_2Cl_{12}$ as photocatalyst

2.4.1 Introduction

Photocatalysis is a term that has been used for nearly 100 years and can be simply described as the change in the rate of a chemical reaction caused by light in the presence of a light-absorbing catalyst that becomes active during the reaction. Although there are so many examples of heterogeneous photocatalysis that span this period, the 1970s were a significant growth period for the field of photocatalysis. During this time, Fujishima and Honda discovered using a semiconducting catalyst and water could be photoelectrochemically split into hydrogen and oxygen. Nanotechnology's ability to solve some of the main problems associated with photocatalysis is the driving force behind this expansion. The challenges include charge isolation, surface area, tunable surface chemistry, the energy of accessible light, and the nature of reactive oxygen species. In recent years, there has been much emphasis on revealing the specifics of TiO_2 photocatalysis since the procedures based on its use are adequate for the decomposition and purifications of various organic and inorganic pollutants found in air, wastewater, and drinking water. When a TiO_2 particle is being subjected to a photon with adequate energy ($E_n > E_{bg}$; E_{bg} = 3.23 eV), the photon's energy is getting absorbed, causing an electron to jump from the valence to the conduction band. A no of holes is getting

generated due to the excitation of electrons in the valence band. Under aerobic conditions, an adsorbed oxygen molecule with a sufficiently high quantum yield traps the conduction band electron, forming an $^{\bullet}O_2^-$ ion that can be protonated in an acidic environment. In the absence of reducing species, the photon-generated void causes surface adsorbed water or hydroxide ion to transform itself into a $^{\cdot}OH$ (hydroxyl radical). The produced active radicals affect the rate of degradation of complex molecules. The rate of degradation reaction can be tuned by varying the surface morphology of catalyst particles.[68]

The DPCl1 compound's bandgap seems to be promising for applications in the fields of photocatalysis. Two sets of reactions were conducted to investigate its photocatalytic activity ferricyanide reduction to ferrocyanide[69] and the degradation of Congo red dye in an ethanolic medium.[70,71]

$$\text{Degradation efficiency (\%)} = [(C_o\text{-}C)/C_o] \times 100$$
$$= [(A_o\text{-}A)/A_o] \times 100$$

The rate constant for the degradation of congo red dye and ferricyanide reduction reaction was obtained from the slope of the pseudo-first-order kinetic plot (C ln C_t / C_0 vs Time). The equation given below can be used to measure the apparent kinetic rate constant (K_{app}) for a given degradation reaction.[72]

$$R = dC/dt = K_{app} \qquad C \ln C_t/C_0 = K_{app}.t$$

'K_{app}' is the apparent kinetic rate constant, 'R' denotes the reaction rate, 't' denotes the reaction time, 'C_0' and 'C_t' is the initial concentration and concentration at the time, t.

2.5 Photocatalysis experiments

2.5.1 Photocatalytic reduction of ferricyanide

2.5.1.1 Synthesis of Solution for Ferricyanide photoreduction reaction

A solution was prepared by dissolving 10 mg potassium ferricyanide and 20 mg DPCl1 photocatalyst in 15 ml ethanol for the photocatalytic reduction reaction. The solution mixture was kept in the dark for 30 min on a running stirrer to achieve the adsorption-desorption equilibrium between the DPCl1 photocatalyst and ferricyanide molecules. After that, the solution transferred to sunlight; the reduction reaction's progress continuously monitored using a UV-vis spectrophotometer. Control experiments were also carried out in dark and daylight to check the photocatalyst behaviour.

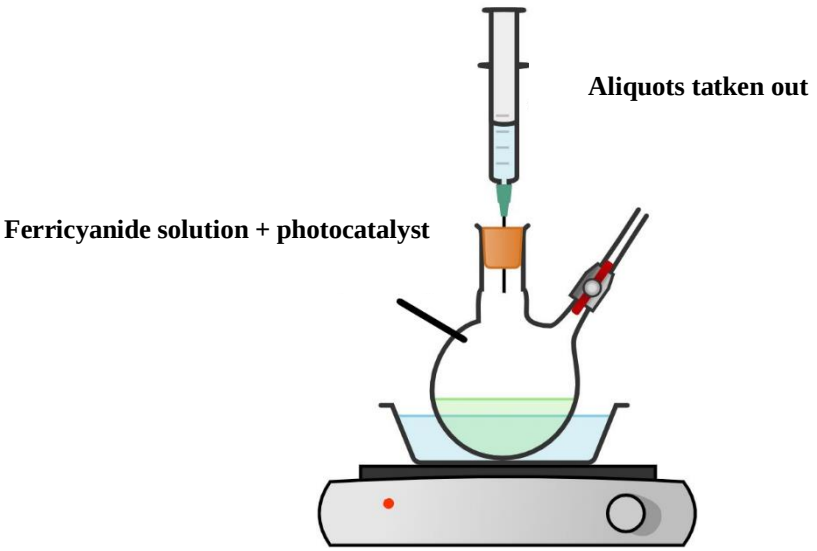

Figure 14. Ferricyanide photocatalytic reduction setup

The photocatalytic reduction reaction of ferricyanide was performed to evaluate the DPC1 Photocatalytic performance under sunlight. An absorption of ferrocyanide at 420 nm was

observed to steadily decrease with a subsequent increase in ferricyanide absorption at 245 nm through the isosbestic point at 285 nm (figure. 15(a)) analyzed by the UV-Vis spectrometer. Instead of this, the colour changes from yellow to colourless., as seen in figure. 15 (c). The reduction takes 20-30 minutes with an 88 % yield of photoconversion using the DPCl1 catalyst. The kinetic study of UV-Vis absorption peak at 420 nm shows that the ferricyanide reduction reaction follows first-order reaction kinetics. The calculated K_{app} for the reduction reaction is 0.092 min^{-1}.

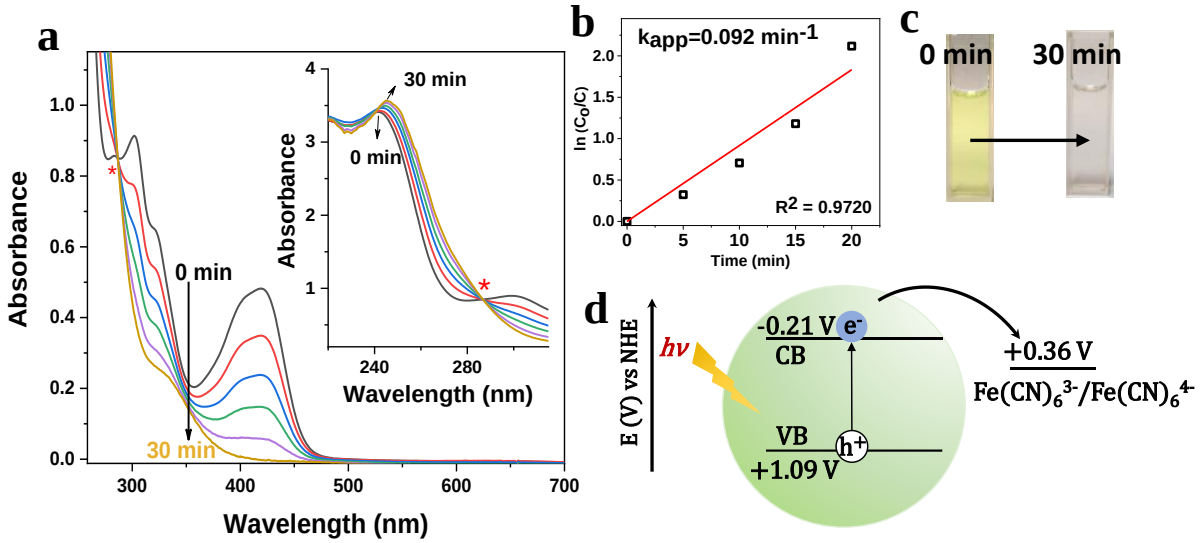

Figure 15. (a) UV-visible spectra of conversion of Fe^{3+} to Fe^{2+} **(b)** Corresponding kinetic plots, **(c)** Digital image of colour transition**, d)** Depicted picture of band positions of catalyst (DPCl1) NCs[66]

2.5.1.2 Mechanism of a photocatalytic ferricyanide reduction reaction

When DPCl1 NCs are exposed to visible light, excitons are produced. The DPCl1 conduction band energy levels (-0.21 V) and the standard reduction potential of the $[Fe(CN)_6]^{3-}$ /$[Fe(CN)_6]^{4-}$ pairs (0.36 V vs SHE) are allowed photo-excited electrons to transition from DPCl1 NC to ferricyanide.[74] The presence of ethanol ensures that the holes collected in the DPCl1 photocatalyst valence band are scavenged, thus assisting the red-ox cycle.

A statistical map was created to illustrate this photocatalyst's efficiency, revealing DPCl1's importance as an efficient photocatalyst. Similarly, DPCl2 photocatalyzed ferricyanide reduction reactions were carried out, and the calculated rate constant was found to be 0.014 min^{-1} which is seven times lower than that of DPCl1.

Table 1: Comparison of apparent ferricyanide reduction constants with hot injection catalysts with other photocatalysts from previous literature.

Photocatalyst	**K_{app} (min^{-1})**
DPCl**1**	9.16×10^{-2}
InP/ZnS QDs[69]	2.70×10^{-2}
15 nm AuNPs@citrate[74]	6.69×10^{-2}
TiO_2 (65%A 35%R)[30]	4.33×10^{2ourf}

The photocatalyst's reusability was suitable for up to four reuse cycles (figure 16a). The PXRD pattern of the photocatalyst was compared before and after the reaction up to four-cycle to confirm the photocatalyst's reusability (figure. 16(a)). It almost retains the PXRD peak, and the recovery of the catalyst was smoother in this manner.

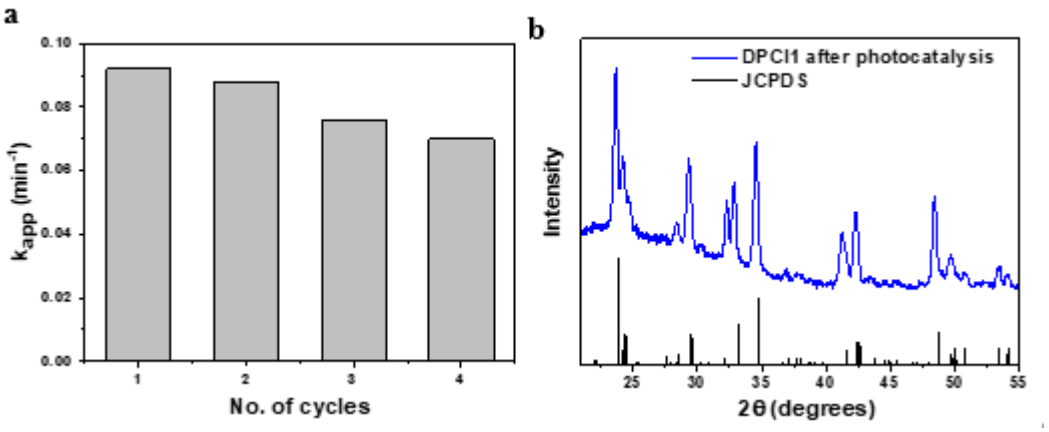

Figure 16. (a) The rate constants for the ferricyanide reduction reaction up to 4 cycles using DPCl1**, (b)** PXRD of the reused catalyst in comparison with JCPDS data for $Cs_4CuSb_2Cl_{12}$[66]

2.5.2 Congo Red dye degradation reaction

We were fascinated by the efficient results of ferricyanide reduction reactions and wanted to see whether $Cs_4CuSb_2Cl_{12}$ could be used as a dye degradation photocatalyst. Congo Red dye was chosen for this purpose.[75] Before starting the congo red dye degradation reaction, the nanocrystals' stability was checked in an aqueous medium, the NCs' initial brownish-black colour faded to white, indicating the compound's instability and toxicity. To overcome these issues, we chose ethanol as a medium.

2.5.2.1 Materials

Congo red (Sigma-Aldrich), Ethanol (Merck Millipore), *t*-butyl alcohol, Coumarin, and ammonium oxalate monohydrate.

2.5.2.2 Solution preparations for Congo Red dye degradation reaction

A Congo red dye photocatalytic experiment was carried out by mixing 6 mg of photocatalyst into 20 ml of Congo red dye (20 mg/L) solution in an ethanolic medium. The whole solution was kept in the dark for 30 minutes, exposed to sunlight.

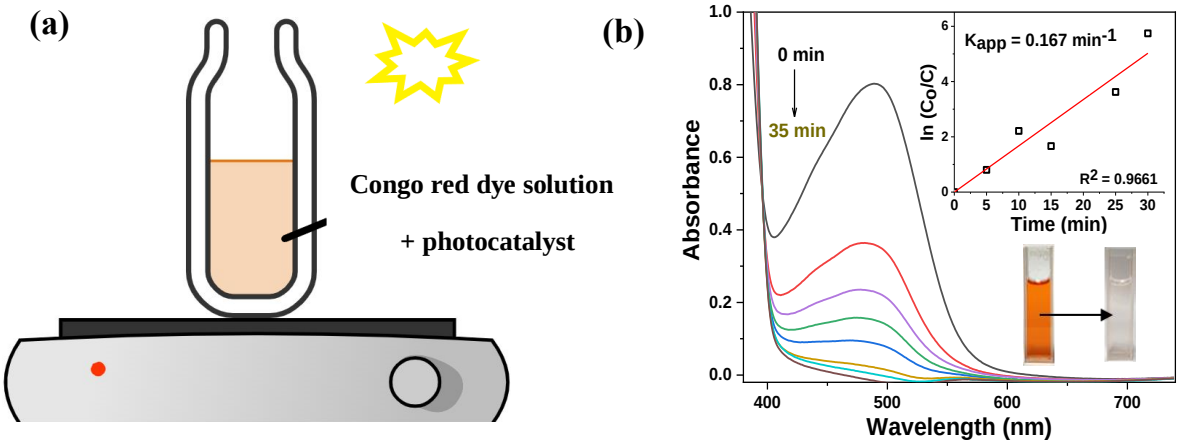

Figure 17. (a) Dye degradation reaction setup and **(b)** UV-visible spectral change, kinetics, colour transition of Congo red[66]

The reaction mixture degradation was monitored by UV-Vis spectroscopy by looking at absorption peak reduction at 500 nm of Congo red dye over time depicted in figure 17b. The Congo red dye's distinguishing peak solution at 500 nm (π–π* transitions of the azo group (–

N≡N–) decreases with time in the presence of DPCl1 and DPCl2 under illumination, as seen in the UV-visible spectra (figure 18).

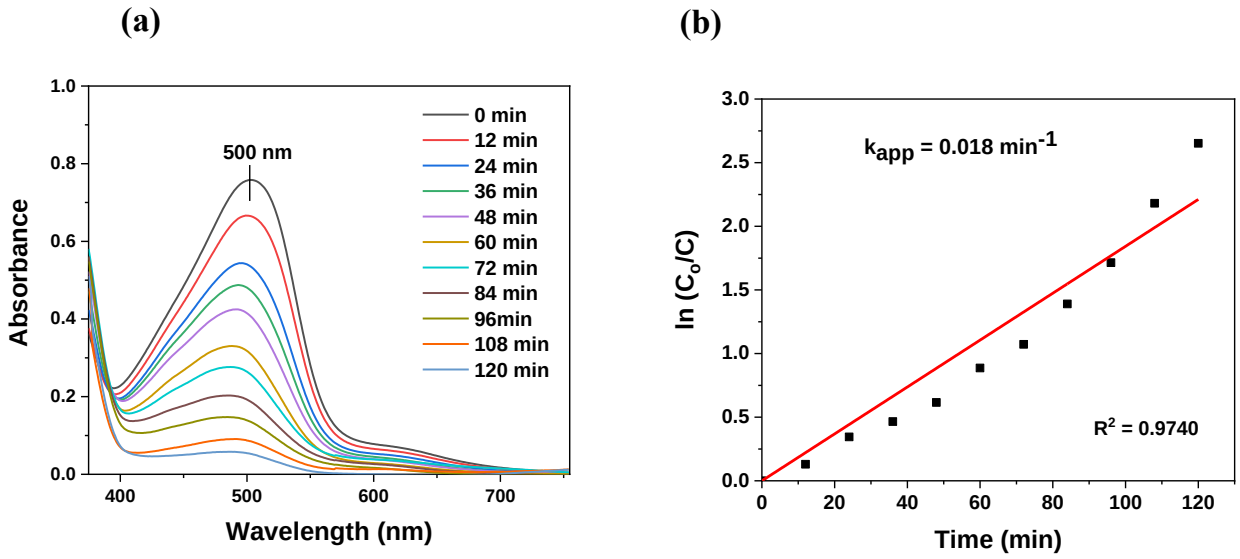

Figure 18. (a) UV-visible spectra of Congo red dye solution in presence of DPCl2 photocatalyst under sunlight, **(b)** corresponding first-order kinetic plot

According to figures 17 and 18, the rate of degradation of DPCl1 photocatalyst is significantly higher than that of DPCl2. Using both the photocatalysts, degradation efficiency was calculated at 99.6% (DPCl1) and 92.95% (DPCl2) in 30 and 120 minutes, respectively. The kinetic studies were done and calculated by the slope of the linear fit graph between the ln (A_o/A) vs. time (t) of the kinetic plot yields a K_{app} of 0.167 min^{-1}.

Table 2: Comparison of apparent rate constants rate of congo red dye degradation with hot injection catalysts with other photocatalysts from previous literature

Photocatalyst	**K_{app} (min^{-1})**
DPCl**1**[66]	1.675 x 10^{-1}
DPCl**2**[66]	1.843 x 10^{-2}
Pure BT material[76]	1.3 x 10^{-2}
CuS_{20}BT[76]	1.45 x 10^{-1}

Copper foam[77]	3.53×10^{-3}
CuO nanowire[77]	5.01×10^{-3}
ZnO@CuO nanostructure[77]	7.12×10^{-3}
Fe_3O_4@CuO nanostructure[77]	7.95×10^{-3}

The reaction with DPCl1 photocatalyst has the highest photocatalytic performance and the calculated kinetic rate constant for congo red dye degradation reaction. The apparent kinetic rate constant for photocatalyst DPCl1 photocatalyst is ten times higher than photocatalyst DPCl2 (mentioned in table 2).

2.5.3 Principle and Mechanism of Congo Red dye degradation Reaction

In a photocatalytic reaction, reactive species may include holes, electrons, hydroxyl, and superoxide radicals. Various equimolar scavengers, such as t-butyl alcohol (hydroxyl radical scavenger), p-benzoquinone ($^{\bullet}O_2^-$, superoxide radical scavenger), and ammonium oxalate (hole scavenger), were added to the reaction medium to clarify the Congo red dye degradation pathway. Figure 20 depicted the kinetic rate comparison of the Congo Red Degradation reaction by using various scavengers. Initially, the ferricyanide absorption peak at 420 nm reduced by half in the presence of t-butyl alcohol as a hydroxyl radical scavenger, but dye solution absorption did not change significantly. Similarly, there was no noticeable reduction in the reaction when ammonium oxalate was used as a hole scavenger, demonstrating that photogenerated holes and hydroxyl radicals are the key species involved in the degradation of the congo red dye, as shown in figure 19.

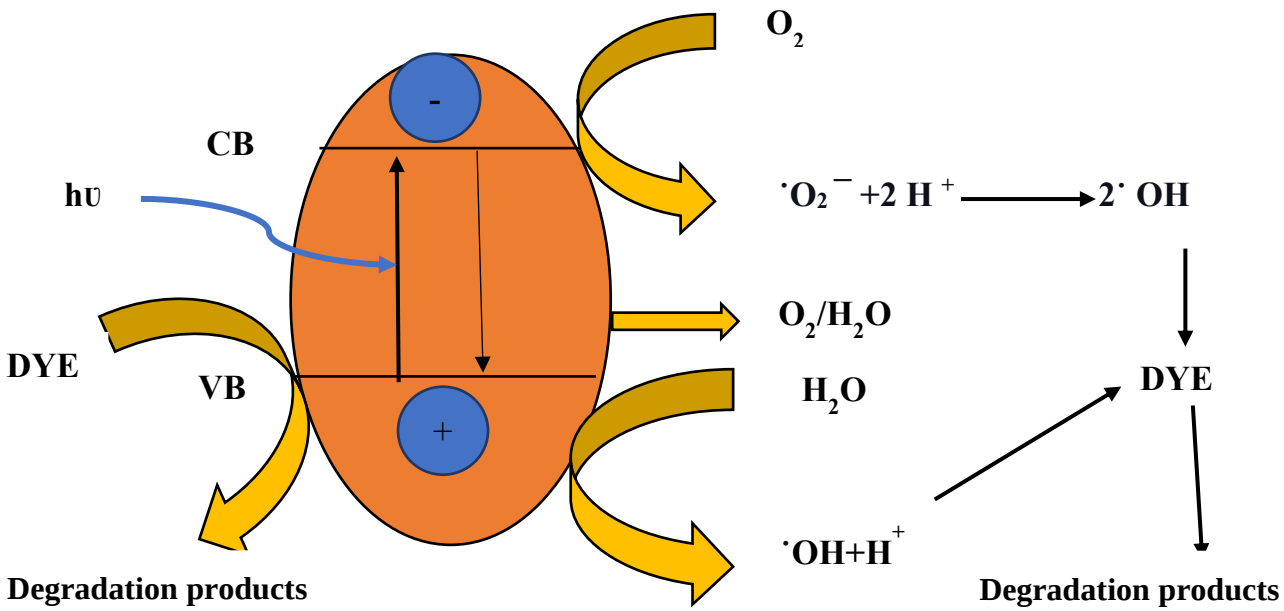

Figure 19. Mechanism of congo red dye degradation reaction

As shown in figure 19, the holes in the VB directly react with the dye (oxidation potential +0.206 V) to produce degradation products. The electrons in the CB transform the surface adsorbed oxygen to superoxide radicals ($^{\bullet}O_2^-$). Despite an ethanolic medium, which can serve as a hole scavenger, the addition of a potent hole scavenger, such as ammonium oxalate, nearly extinguishes the reaction for a brief period, meaning that the hole plays a vital role in dye degradation. $^{\bullet}O_2^-$ can also form hydrogen peroxide (H_2O_2) in the presence of organic scavengers by reacting with two H^+ ions and then converting to $^{\cdot}OH$. These $^{\cdot}OH$, hydroxyl radicals control dye degradation reaction. The existence of $^{\cdot}OH$ was confirmed by adding t-butyl alcohol to the reaction mixture, which revealed that degradation was minimal in the presence of t-butyl alcohol $^{\cdot}OH$.

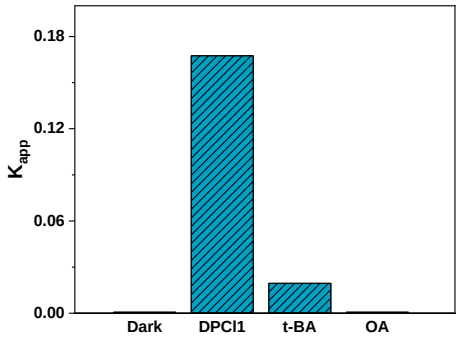

Figure 20. Degradation rates for Congo red dye with photocatalyst, radical scavengers, and under dark

2.5.4 Using coumarin as a fluorescent probe for hydroxyl radical (˙OH) detection

Coumarin was used as a fluorescent probe to detect hydroxyl radical (˙OH). Coumarin reacts with ˙OH hydroxyl radicals to form the fluorescent derivative 7-hydroxy coumarin, which emits at 455nm.[78]

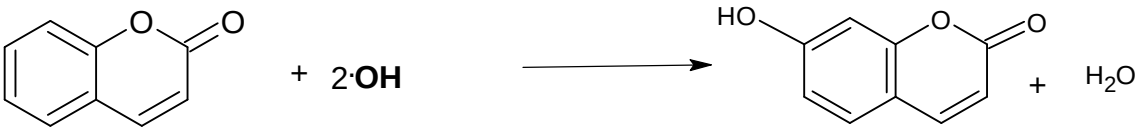

Coumarin (COU) 7-hydroxycoumarin(7HC)

2.5.4.1 Materials

Ethanol (Merck Millipore); *t*-butyl alcohol; Coumarin; and ammonium oxalate monohydrate, Silver nitrate ($AgNO_3$, Sigma-Aldrich), Oxalic acid (Sigma-Aldrich).

2.5.4.2 Coumarin Solution preparations to detect ˙OH (hydroxyl radical)

A photocatalyst (1mg/ml) was suspended in 10^{-4}M ethanolic coumarin solution to conduct this experiment. The dye molecules and the photocatalyst were left in the dark for 30 minutes to reach adsorption-desorption equilibrium; after that, the whole solution is transferred to sunlight.

In the first example, $AgNO_3$ (concentrations ranging from 10^{-4}M to 10^{-5} M) was used as an electron acceptor, while oxalic acid (concentrations ranging from 10^{-4} M) was used as an electron donor in addition to $AgNO_3$. The reaction vials were then purged with N_2 gas to create anaerobic conditions under sunlight, with aliquots taken at predetermined time intervals. Indeed, emission at 455 nm occurs in the first case, indicating the formation of 7-hydroxy coumarin, and emission intensity was found to increase with increasing Ag ion concentration in the 10^{-5} to 10^{-4} M range depicted in figure 21(a). Figure 21 shows an increase in luminescence strength is accompanied by a levelling off after 10-20 minutes of irradiation at both Ag^+ ion concentrations.

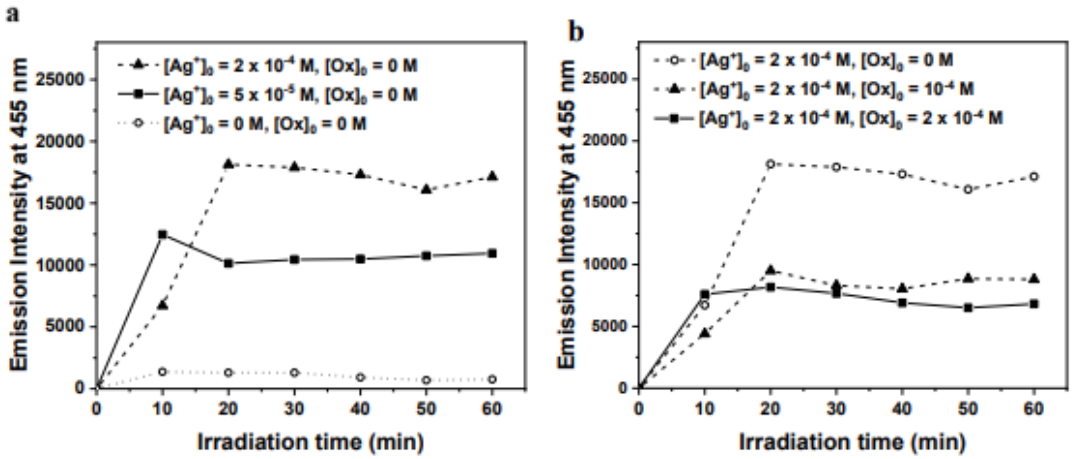

Figure 21. Development of fluorescent peak at 455 nm in the photocatalytic reaction mixture of 1 mg/ml of DPCl1 photocatalyst, 10^{-4} M coumarin, and **(a)**various concentration of Ag^+ under sunlight, **(b)** 2×10^{-4} M $AgNO_3$, and various concentration of oxalic acid under sunlight[66]

In the second case, adding an appropriate electron donor to the reaction mixture, such as oxalic acid, along with $AgNO_3$, decreases the strength of the hydroxy coumarin fluorescence signal (figure 21 (b)). Oxalic acid prevents the development of fluorescent 7-hydroxy coumarin by scavenging the holes. As a result, it is concluded that active species such as hydroxyl radicals, in conjunction with the holes formed, cause the Congo red dye to degrade.

2.5.4.3 A mechanism for the detection of ˙OH (hydroxyl radical)

Electrons transfer from the excited photocatalyst's conduction band to silver ions when exposed to sunlight, resulting in Ag deposition on the photocatalyst's surface. Since this

reaction produces no radicals, a favourable environment for transferring the holes from CB to the hydroxide ion forming the ˙OH (hydroxyl radical) can be generated. These ˙OH hydroxyl radicals react with coumarin, and 7- hydroxyl-coumarin formed.[78] The formation of hydroxy coumarin is halted once the Ag atoms deposited, as evidenced by the flattening of the 455 nm emission intensity. Different scavengers were used to monitor the quantity of ˙OH hydroxyl radicals formation.

Chapter 3

Project 2. Copper doping on 2D perovskite $(BA)_2PbCl_4$ and its photocatalytic activity

Experimental section

3.1 Materials

Lead Chloride ($PbCl_2$, 99%, Alfa Aesar), Copper (II) chloride dehydrate ($CuCl.2H_2O$, 99%, Sigma Aldrich), Butylamine ($C_4H_9NH_3$, 99%), 1-Octadecene (ODE, 90 %), Hydrochloric acid (HCl, 37%, Emparta).

3.2 Synthesis of undoped $(BA)_2PbCl_4$ and Cu^+, Cu^{2+} doped $(BA)_2PbCl_4$

3.2.1 Synthesis of undoped $(BA)_2PbCl_4$

Before the synthesis of undoped and Cu^+, Cu^{2+} doped $(BA)_2PbCl_4$, BACL (Butylammonium Chloride salt) salt was prepared, depicted in figure 22.

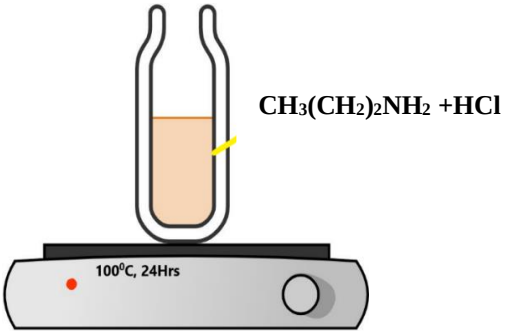

Figure 22. Synthesis of BACl (butylammonium chloride) salt

For the synthesis of undoped $(BA)_2PbCl_4$, 27.8mg of $PbCl_2$, 58.0mg of BACl, 0.3ml of HCl, 5ml of ODE were mixed together in a 50ml Schlenk flask and heated at 120^0C under a dry N_2 atmosphere for 15min. After completing the reaction, Cooldown it to room temperature keeping it outside for an hour; the solution was mixed with 6ml ethyl acetate (antisolvent), centrifuge it at 2000rpm for 2min. The supernatant was discarded, and the precipitate washed twice with 2ml of hexane. Finally, filtered it out by using Buckner funnel, and white-coluored crystals were obtained.

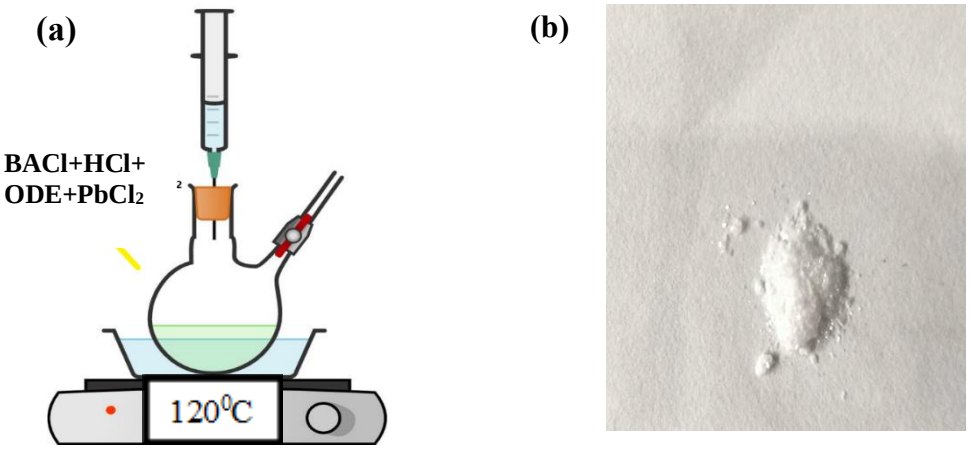

Figure 23. (a) Synthesis of undoped $(BA)_2PbCl_4$ NCs, **(b)** colorless undoped $(BA)_2PbCl_4$ NCs

3.2.2 Synthesis of Cu^{+} and Cu^{2+} doped $(BA)_2PbCl_4$

For the synthesis of Cu^{+} and Cu^{2+} doped $(BA)_2PbCl_4$; 27.8mg of $PbCl_2$, 58.0mg of BACl, CuCl ($CuCl_2.2H_2O$),0.3ml of HCl, 5ml of ODE were mixed in 50ml Schlenk flask and heated at 120c under dry N_2 atmosphere for 15min. After completing the reaction, Cooldown it to room temperature keeping it outside for an hour; the solution was mixed with 6ml ethyl acetate (antisolvent), centrifuge it at 2000rpm for 2min. The supernatant was discarded, and the precipitate particles washed twice with 2ml of hexane. Finally, filtered it out by using Buckner funnel, and yellow-coloured crystals were obtained.

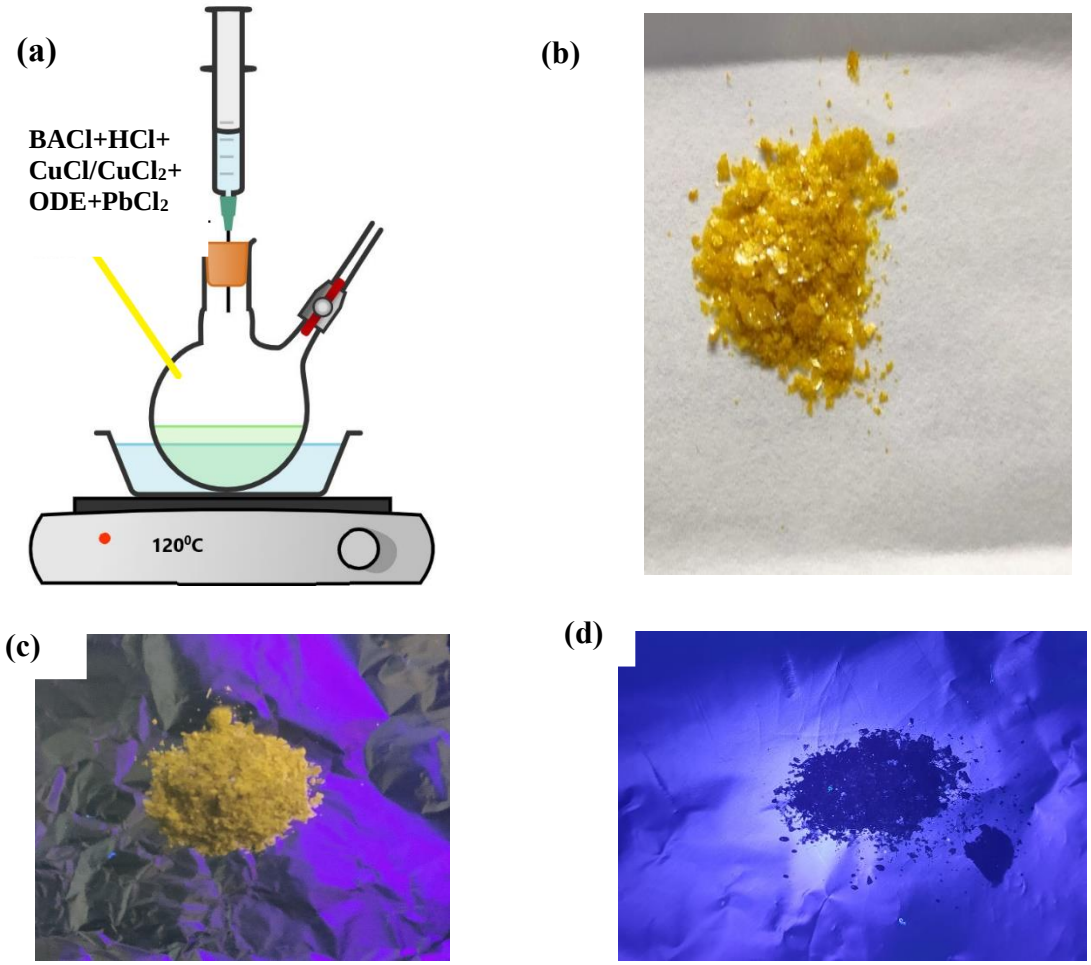

Figure 24. (a) Synthesis of Cu^{+} doped $(BA)_2PbCl_4$ NCs, Cu^{2+}doped crystals in **(b)** normal light, digital image in UV light of **(c)** at wavelength 365, **(d)** at wavelength 254nm

3.3 Result and discussion

The XRD peaks show that the crystals formed have good crystallinity and purity and are oriented along the c-axis direction. With the addition of copper, new peaks begin to appear at lower angles. The intensities of the original peaks in the undoped system decrease with copper doping.[79]

The XPS data of the copper doped sample shows the same pattern of high satellite peaks, suggesting a Cu^{2+} oxidation state for both Cu^{+} doped $(BA)_2PbCl_4$ and Cu^{2+} doped $(BA)_2PbCl_4$. The EPR signal has a peak at 3130 Gauss that corresponds to the presence of Cu^{2+} in the sample. Cu^{+} doped $(BA)_2PbCl_4$ and Cu^{2+} doped $(BA)_2PbCl_4$ have identical EPR peak positions, supporting the electronic and coordination environment similarities. There was no evidence of hyperfine splitting, implying contact between the Cu (II) centers of the doped system with total electron spin s=1/2.

The organic component of the undoped and copper-doped samples is verified using FT-IR spectroscopy.

The Tauc plot is used to determine the optical bandgap of materials. The determined bandgap for $(BA)_2PbCl_4$ is around 3.52eV;[80]; however, after Cu^{+} and Cu^{2+} doping, the bandgap is reduced to 2.3eV and 2.27eV, respectively. The bandgap here indicates to be favourable for a reaction triggered by sunlight. Figure 25 shows how the bandgap varies with copper doping.

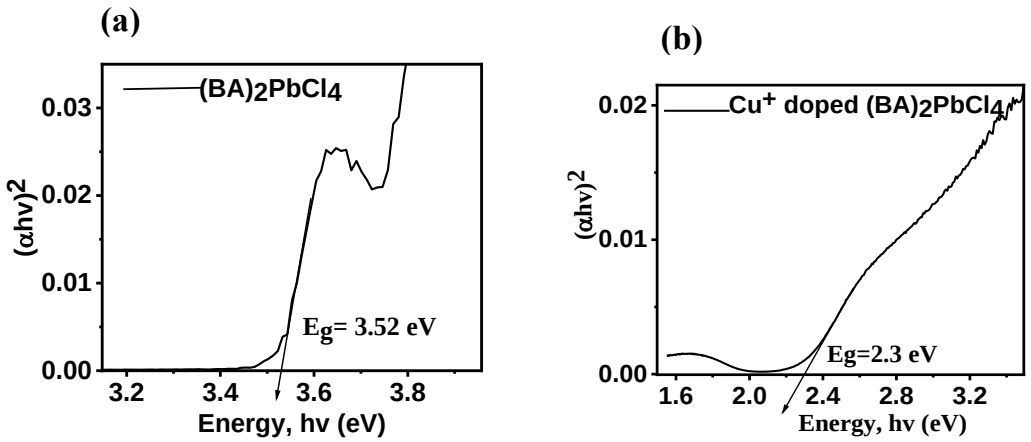

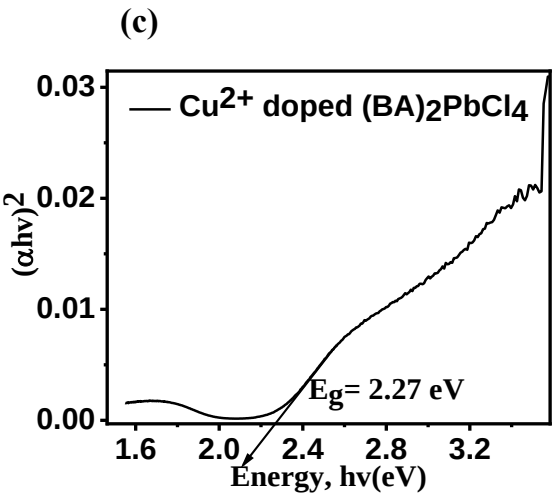

Figure 25. Tauc plot of **(a)** Undoped $(BA)_2PbCl_4$, **(b)** Cu^+, **(c)** Cu^{2+} doped $(BA)_2PbCl_4$

TGA of undoped $(BA)_2PbCl_4$ and Cu^{2+} doped $(BA)_2PbCl_4$ was performed to investigate the impact of doping on system stability. TGA revealed that the thermal decomposition temperature of the Cu^{2+} doped system was slightly higher than that of pure $(BA)_2PbCl_4$. DSC studies on the perovskite were undertaken, demonstrating structural transitions below the melting/decomposition point. Here the sample was heated from -10°C to 190°C and then cooled back down to -10°C. Figure 26 depicts the DSC data for the NCs.

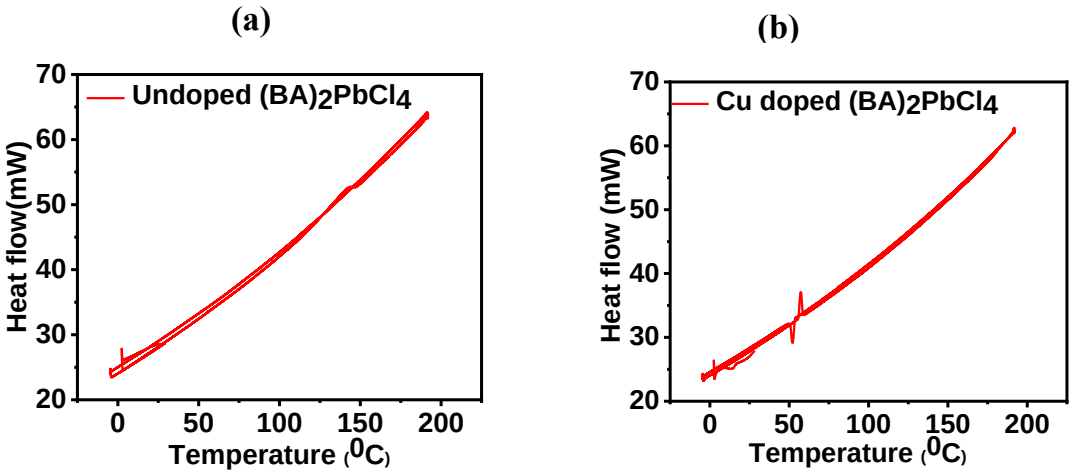

Figure 26. DSC Analysis of **(a)** undoped $(BA)_2PbCl_4$, **(b)** Cu doped $(BA)_2PbCl_4$

In the DSC curve, the phase transition at 51^0C corresponds to a solid-solid phase transition, and its enthalpy and entropy changes are H = 34.19 kJ mol−1 and S = 105.39 J K−1 mol−1, respectively. Below 51^0C, the organic chain is ordered and contains the all-trans alkyl

conformation, and beyond the temperature, the conformations of the alkyl chains become disordered. Therefore, the transition at 51^0C originates from the order-disorder growth of the alkylammonium cation.

The valence band maximum (VBM) position and the effective work function are calculated by ultraviolet photoelectron spectroscopy (UPS), which, when combined with the bandgap value obtained, yields the minimum position of the conduction band. The VBM location is approximately 2.89 eV lower than the Fermi stage. It depicts a graphical representation of the band structure with an optical band gap of 2.27 eV.

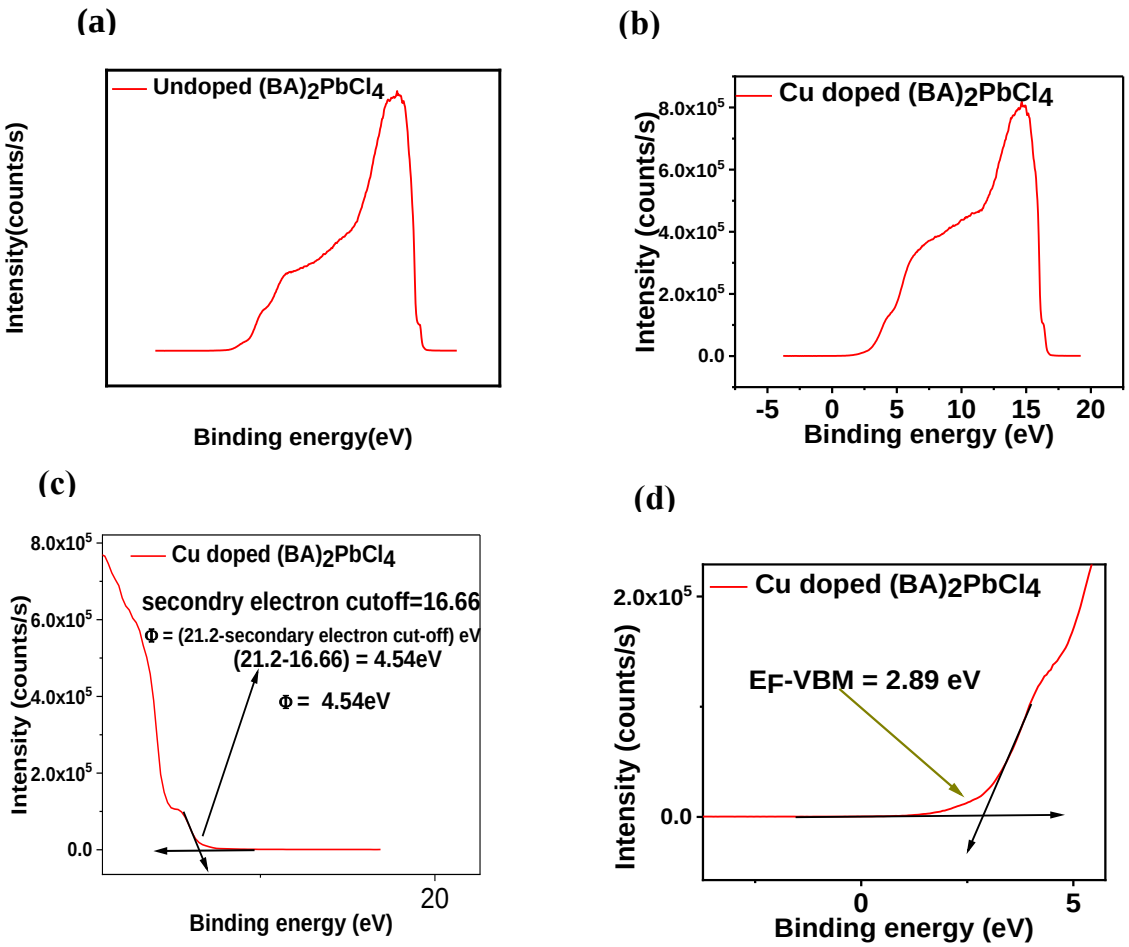

Figure 27. UPS Analysis of **(a)** undoped $(BA)_2PbCl_4$, **(b,c,d)** Cu^{2+} doped $(BA)_2PbCl_4$

3.4 Application of Cu^{2+} Doped $(BA)_2PbCl_4$ double perovskite as photocatalyst

3.4.1 Introduction

Heterogeneous photocatalysis was shown to be an effective method for degrading organic pollutants in both the atmosphere and water.[82] It employs sunlight in the presence of a semiconductor photocatalyst to speed up the removal of chemical pollutants and the degradation of highly toxic molecules. In photocatalysis reaction, the nanocrystals with harmful contaminants in solution were stimulated by photons with sufficient energy; thus, electron and hole (exciton) were produced in the conduction band and valence band, respectively. These electrons and holes take part in photocatalysis reaction and produce active radicals on the surface of the photocatalyst or in the solution[83] that helps in the degradation and reduction of toxic complex molecules like organic dye.

3.4.2 Photocatalytic degradation of congo red dye

3.4.2.1 Congo red dye degradation reaction using a photocatalyst

The photocatalytic behaviour of Cu^{2+} doped $(BA)_2PbCl_4$ was investigated by analyzing the apparent kinetic rate constant of congo red dye under sunlight. Initially, a stock solution of 4mg of congo red dye, dissolved in 10 mL of ethanol, was prepared and then diluted ten times. 18 mg of the photocatalyst was applied to 10 ml of the diluted stock solution and held in sunlight with constant stirring. Different sets of the reaction were held for different periods (aliquots taken at 5min intervals). The reaction mixture after extracting the photocatalyst was taken for further investigation by recording UV-Vis spectra, as shown in figure 28.

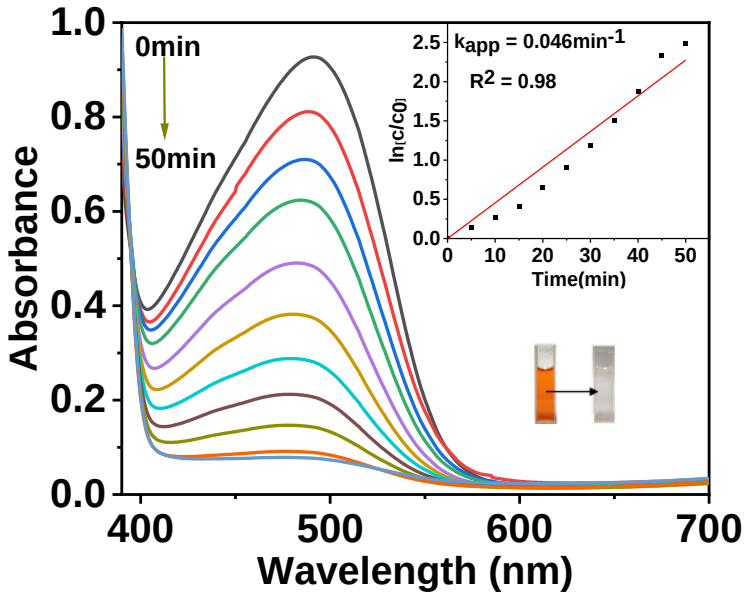

Figure 28. UV-visible spectral change of Congo red dye solution in presence of Cu^{2+} doped $(BA)_2PbCl_4$ photocatalyst under sunlight, inset corresponding kinetic plot, colour transition

3.4.2.2 Congo red dye degradation reaction using photocatalyst in the presence of t-Butyl Alcohol

After looking at the congo red dye degradation using the photocatalyst, we used t-butyl alcohol as a hydroxyl radical scavenger. Initially, the same reaction condition was provided here: a stock solution of 4mg of congo red dye, dissolved in 10 mL of ethanol, prepared and diluted ten times. 18 mg of the photocatalyst and 1ml of t-butyl alcohol were applied to 10 ml of the diluted stock solution and put in the dark for 15 min to achieve the adsorption-desorption equilibrium state between dye molecules and photocatalyst. The whole solution was then transferred to sunlight. Different sets of the reaction were held for different periods (5min, 10min, 15min, 20min, 25min, 30min). The reaction mixture after extracting the photocatalyst was taken for further investigation by recording UV-Vis spectra, as shown in figure 29.

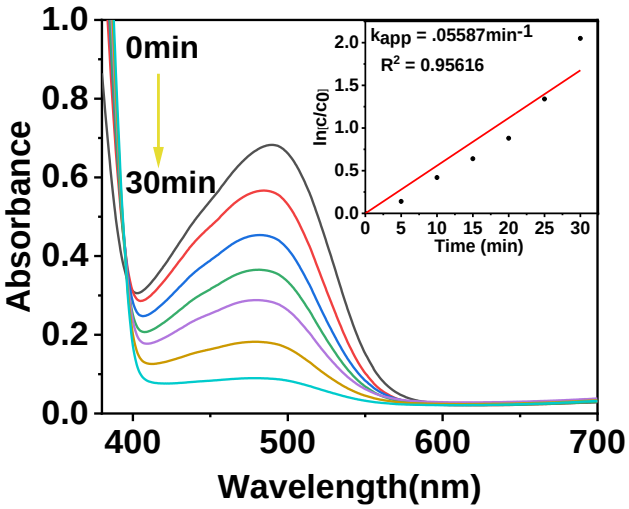

Figure 29. UV-visible spectra of Congo red dye solution in presence of Cu^{2+} doped $(BA)_2PbCl_4$ and t- butyl alcohol (hydroxyl scavenger) under sunlight, inset corresponding kinetic plot.

3.4.2.3 Control experiments

In controlled photocatalysis, the congo red dye degradation in the absence of sunlight and photocatalyst has also been studied to compare the above results.

Without a photocatalyst, the congo red dye does not degrade in sunlight. It shows that Cu^{2+} doped $(BA)_2PbCl_4$ can be used as a photocatalyst

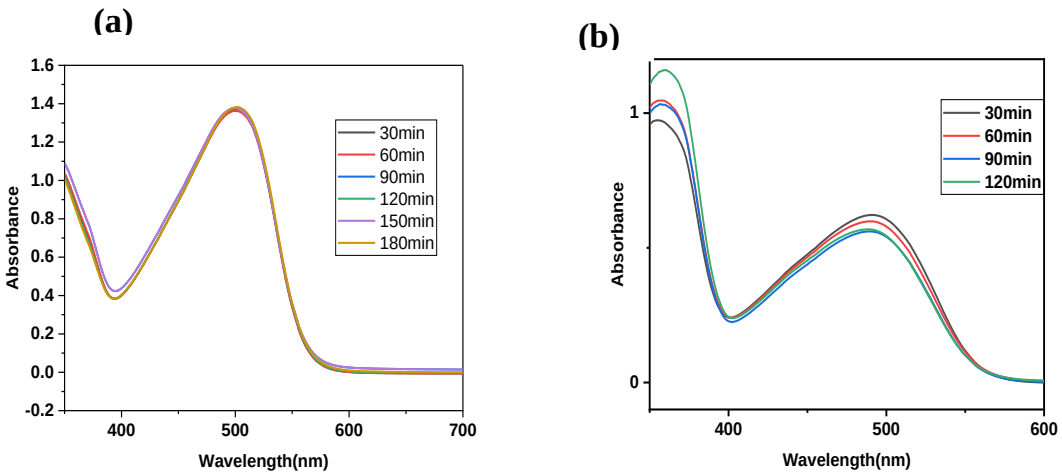

Figure 30. Congo red dye degradation **(a)** without photocatalyst in the presence of sunlight **(b)** with photocatalyst in dark

3.4.2.4 Mechanism of congo red dye degradation using Cu^{2+} doped $(BA)_2PbCl_4$

Further studies include understanding the mechanism and confirming the photocatalytic activity through various photocatalytic reactions. As already discussed, the major active species involved in a photocatalytic process are the VB holes, CB electrons, ˙OH (hydroxyl radicals), and superoxide radicals anion ($^{\bullet}O_2^-$). It is necessary to identify the active species mainly involved in the photocatalytic reaction to evaluate the photodegradation mechanism of congo red dye. For that purpose, various active species scavengers such as t-butyl alcohol (˙OH, hydroxyl radical scavenger), p-benzoquinone (superoxide radical scavenger), and ammonium oxalate (hole scavenger) need to be used in the reaction medium to ascertain the congo red dye degradation pathway. Figures 28 and 29 depict UV-Vis spectra of congo red dye degradation in the absence and presence of t-butyl alcohol. The kinetics rate comparison bar diagram figure 31(a) shows that the degradation rate significantly enhances around ten times in the presence of hydroxyl scavenger (t-butyl alcohol).

(a)

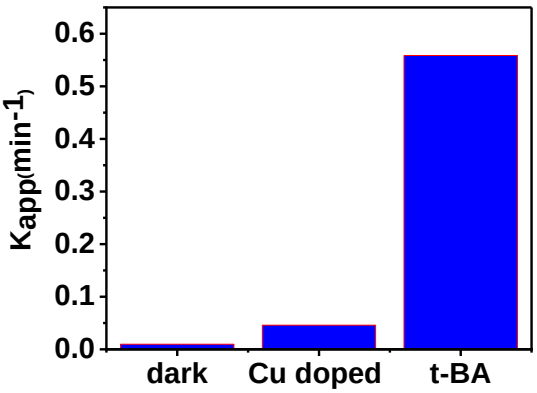

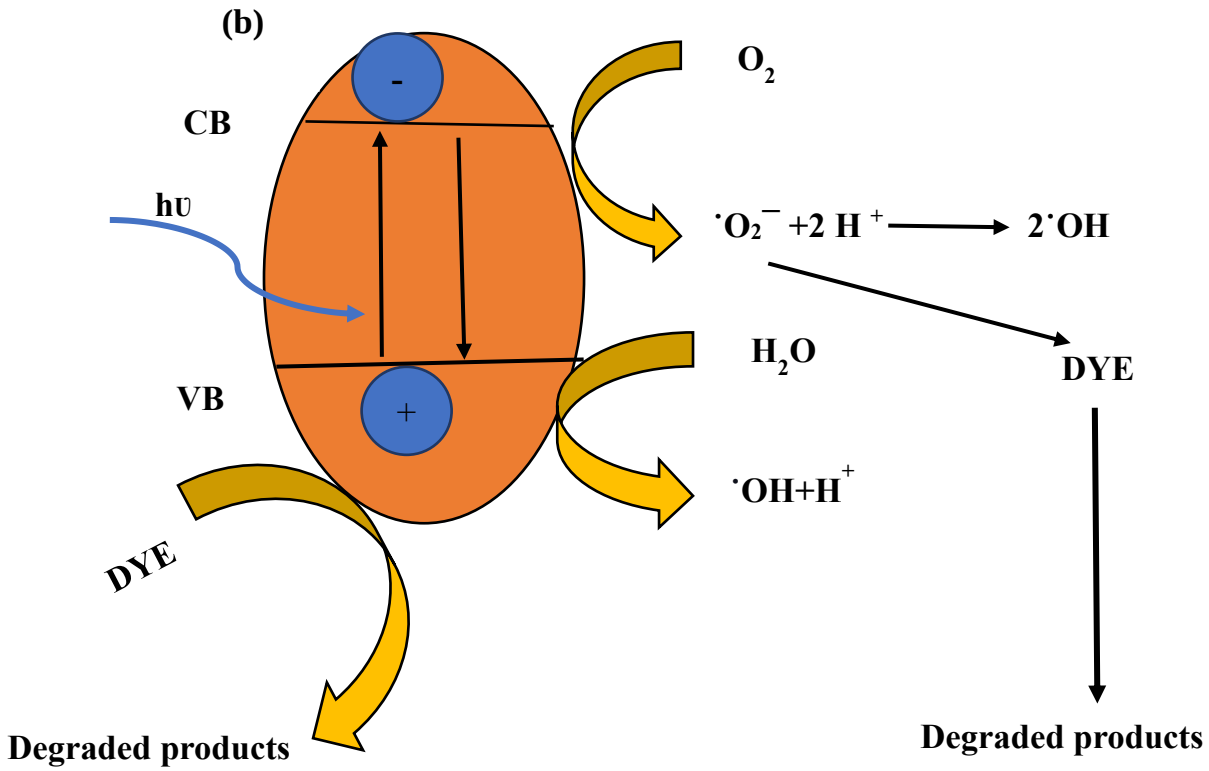

Figure 31. (a) Degradation rates for Congo-red dye using photocatalyst Cu^{2+} doped $(BA)_2PbCl_4$ in dark, sunlight, hydroxyl radical scavengers **(b)** mechanism of dye degradation

The degradation rate is faster in the presence of hydroxyl scavenger depicted in figures 31(a) and (b), showing the ˙OH (hydroxyl radical) is not an active species in the degradation reaction. From this, we conclude that either electron, superoxide radical anion, or some other active species drives the degradation reaction. Further studies need to be done using different scavengers to know which active species is involved in congo red dye degradation.

Conclusions and Future Outlook

Conclusions

Project 1

2D layered $Cs_4CuSb_2Cl_{12}$ has been successfully synthesized using hot injection method and acid-mediated solution-phase synthetic route. $Cs_4CuSb_2Cl_{12}$ nanocrystals with unit cell thickness and a lower bandgap value (1.3eV-1.6eV) exhibit high absorption in the visible range. They can thus be used as an excellent photovoltaic absorber and a visible-light-driven photocatalyst. Photocatalytic reactions carried out using $Cs_4CuSb_2Cl_{12}$ and photocatalysts revealed that $Cs_4CuSb_2Cl_{12}$ shows excellent photocatalytic activity for ferricyanide redox and congo red dye degradation reactions. Furthermore, the nanocrystals' catalytic nature provides new knowledge about their surface properties and other efficient chemical reactions. The higher photocatalytic activity of DPCl1 nanocrystal compared to DPCl2 microcrystal photocatalyst for both ferricyanide reduction and dye degradation reactions could be attributed to DPCl1's smaller crystalline scale, which results in higher surface area and provides a greater number of photo-catalytically active sites. The obtained $Cs_4CuSb_2Cl_{12}$ NCs is discovered to be more efficient for visible-light-driven photocatalytic reaction than their micron-scale counterparts.

Project 2

In the 2D Ruddlesden popper series, synthesis of organic-inorganic lead halide perovskite $(BA)_2PbCl_4$ and copper doping was successfully achieved using the solution phase method. TGA and DSC result shown high thermal stability. The Tauc plot shows that after copper doping of$(BA)_2PbCl_4$, the bandgap is reduced from 3.58eV to 2.27eV and falls within the

visible range, making it a strong candidate photovoltaic absorber and sunlight-driven photocatalyst.

Future Outlook

Cu^{2+} Doped $(BA)_2PbCl_4$ NCs exhibit low bandgap, which can be utilized for deriving different photocatalytic degradation reactions. Just as doped $(BA)_2PbCl_4$ NCs are shown to have efficient photocatalytic activity for Congo red dye degradation, its activities toward other photocatalytic reactions can be studied. It is always necessary to identify the active species mainly involved in the photocatalytic reaction. To that end, various active species scavengers need to be used in the reaction to monitor whether a drastic change in the photodegradation rate is observed.

Bibliography

(1) Kühn, G. O. Muller, R. Roy. The Major Ternary Structural Families. Crystal Chemistry of Non-Metallic Materials. Editor: R. Roy. Vol. 4 Springer-Verlag Berlin-Heidelberg-New York 1974. IX, 487 Seiten, 46 Abbildungen, Zahlreiche Tabellen, Leinen, Preis Geb. DM 76,–; US $ 31,10. *Cryst. Res. Technol.* **1975**, *10* (7), K86–K86.

(2) Köhler, J. Inorganic Solid Fluorides. Chemistry and Physics. Herausgegeben von P. Hagenmüller. Academic Press, New York 1985. XV, 628 S., Geb. $ 99.00. — ISBN 0-12-313380-X. *Angew. Chem. Weinheim Bergstr. Ger.* **1987**, *99* (7), 724–725.

(3) Zhao, X.; Park, N.-G. Stability Issues on Perovskite Solar Cells. *Photonics* **2015**, *2* (4), 1139–1151.

(4) Travis, W.; Glover, E. N. K.; Bronstein, H.; Scanlon, D. O.; Palgrave, R. G. On the Application of the Tolerance Factor to Inorganic and Hybrid Halide Perovskites: A Revised System. *Chem. Sci.* **2016**, *7* (7), 4548–4556.

(5) Jain, M.; Singh, A.; Basera, P.; Kumar, M.; Bhattacharya, S. Understanding the Role of Sn Substitution and Pb-□ in Enhancing the Optical Properties and Solar Cell Efficiency of CH(NH2)2Pb1−x−ySnx□yBr3. *J. Mater. Chem. C Mater. Opt. Electron. Devices* **2020**, *8* (30), 10362–10368.

(6) Park, N.-G. Halide Perovskite Photovoltaics: History, Progress, and Perspectives. *MRS Bull.* **2018**, *43* (7), 527–533.

(7) Huynh, K. A.; Nguyen, D. L. T.; Nguyen, V.; Vo, D. N.; Trinh, Q. T.; Nguyen, T. P.; Kim, S. Y.; Van Le, Q. Halide Perovskite Photocatalysis: Progress and Perspectives. *J. Chem. Technol. Biotechnol.* **2020**, No. jctb.6342. https://doi.org/10.1002/jctb.6342.

(8) Huang, H.; Pradhan, B.; Hofkens, J.; Roeffaers, M. B. J.; Steele, J. A. Solar-Driven Metal Halide Perovskite Photocatalysis: Design, Stability, and Performance. *ACS Energy Lett.* **2020**, *5* (4), 1107–1123.

(9) Gualdrón-Reyes, A. F.; Rodríguez-Pereira, J.; Amado-González, E.; Rueda-P, J.; Ospina, R.; Masi, S.; Yoon, S. J.; Tirado, J.; Jaramillo, F.; Agouram, S.; Muñoz-Sanjosé, V.; Giménez, S.; Mora-Seró, I. Unravelling the Photocatalytic Behavior of All-Inorganic Mixed Halide Perovskites: The Role of Surface Chemical States. *ACS Appl. Mater. Interfaces* **2020**, *12* (1), 914–924.

(10) Unger, E. L.; Kegelmann, L.; Suchan, K.; Sörell, D.; Korte, L.; Albrecht, S. Roadmap and Roadblocks for the Band Gap Tunability of Metal Halide Perovskites. *J. Mater. Chem. A Mater. Energy Sustain.* **2017**, *5* (23), 11401–11409.

(11) Vogt, C.; Groeneveld, E.; Kamsma, G.; Nachtegaal, M.; Lu, L.; Kiely, C. J.; Berben, P. H.; Meirer, F.; Weckhuysen, B. M. Unravelling Structure Sensitivity in CO2 Hydrogenation over Nickel. *Nat. Catal.* **2018**, *1* (2), 127–134.

(12) Zhu, K.; Ju, Y.; Xu, J.; Yang, Z.; Gao, S.; Hou, Y. Magnetic Nanomaterials: Chemical Design, Synthesis, and Potential Applications. *Acc. Chem. Res.* **2018**, *51* (2), 404–413.

(13) Assirey, E. A. R. Perovskite Synthesis, Properties and Their Related Biochemical and Industrial Application. *Saudi Pharm. J.* **2019**, *27* (6), 817–829.

(14) Singhal, N.; Chakraborty, R.; Ghosh, P.; Nag, A. Low-Bandgap Cs4CuSb2Cl12 Layered Double Perovskite: Synthesis, Reversible Thermal Changes, and Magnetic Interaction. *Chem. Asian J.* **2018**. https://doi.org/10.1002/asia.201800635.

(15) Kulkarni, S. A.; Mhaisalkar, S. G.; Mathews, N.; Boix, P. P. Perovskite Nanoparticles: Synthesis, Properties, and Novel Applications in Photovoltaics and LEDs. *Small Methods* **2019**, *3* (1), 1800231.

(16) Wang, S.; Wang, K.; Gu, Z.; Wang, Y.; Huang, C.; Yi, N.; Xiao, S.; Song, Q. Solution-Phase Synthesis of Cesium Lead Halide Perovskite Microrods for High-Quality Microlasers and Photodetectors. *Adv. Opt. Mater.* **2017**, *5* (11), 1700023.

(17) Fathi-Achachelouei, M.; Knopf-Marques, H.; Ribeiro da Silva, C. E.; Barthès, J.; Bat, E.; Tezcaner, A.; Vrana, N. E. Use of Nanoparticles in Tissue Engineering and Regenerative Medicine. *Front. Bioeng. Biotechnol.* **2019**, *7*, 113.

(18) Antony K. J., I.; Jana, D. Stable Mn-Doped CsPbCl3 Nanocrystals inside Mesoporous Alumina Films for Display and Catalytic Applications. *ACS Appl. Nano Mater.* **2020**, *3* (3), 2941–2951.

(19) Takhellambam, D.; Meena, T. R.; Jana, D. Room Temperature Synthesis of Blue and Green Emitting CsPbBr3 Perovskite Nanocrystals Confined in Mesoporous Alumina Film. *Chem. Commun. (Camb.)* **2019**, *55* (33), 4785–4788.

(20) Lee, M. M.; Teuscher, J.; Miyasaka, T.; Murakami, T. N.; Snaith, H. J. Efficient Hybrid Solar Cells Based on Meso-Superstructured Organometal Halide Perovskites. *Science* **2012**, *338* (6107), 643–647.

(21) Williamson, B. W.; Eickemeyer, F. T.; Hillhouse, H. W. Solution-Processed BiI3 Films with 1.1 EV Quasi-Fermi Level Splitting: The Role of Water, Temperature, and Solvent during Processing. *ACS Omega* **2018**, *3* (10), 12713–12721.

(22) Schileo, G.; Grancini, G. Lead or No Lead? Availability, Toxicity, Sustainability and Environmental Impact of Lead-Free Perovskite Solar Cells. *J. Mater. Chem. C Mater. Opt. Electron. Devices* **2021**, *9* (1), 67–76.

(23) Mahesh, K. P. O.; Chang, C.-Y.; Hong, W.-L.; Wen, T.-H.; Lo, P.-H.; Chiu, H.-Z.; Hsu, C.-L.; Horng, S.-F.; Chao, Y.-C. Lead-Free Cesium Tin Halide Nanocrystals for Light-Emitting Diodes and Color down Conversion. *RSC Adv.* **2020**, *10* (61), 37161–37167.

(24) Yin, W.-J.; Shi, T.; Yan, Y. Superior Photovoltaic Properties of Lead Halide Perovskites: Insights from First-Principles Theory. *J. Phys. Chem. C Nanomater. Interfaces* **2015**, *119* (10), 5253–5264.

(25) Pal, J.; Manna, S.; Mondal, A.; Das, S.; Adarsh, K. V.; Nag, A. Colloidal Synthesis and Photophysics of M3 Sb2 I9 (M=cs and Rb) Nanocrystals: Lead-Free Perovskites. *Angew. Chem. Int. Ed Engl.* **2017**, *56* (45), 14187–14191.

(26) Saparov, B.; Hong, F.; Sun, J.-P.; Duan, H.-S.; Meng, W.; Cameron, S.; Hill, I. G.; Yan, Y.; Mitzi, D. B. Thin-Film Preparation and Characterization of Cs3Sb2I9: A Lead-Free Layered Perovskite Semiconductor. *Chem. Mater.* **2015**, *27* (16), 5622–5632.

(27) Giustino, F.; Snaith, H. J. Toward Lead-Free Perovskite Solar Cells. *ACS Energy Lett.* **2016**, *1* (6), 1233–1240.

(28) Pal, J.; Bhunia, A.; Chakraborty, S.; Manna, S.; Das, S.; Dewan, A.; Datta, S.; Nag, A. Synthesis and Optical Properties of Colloidal M3Bi2I9 (M = Cs, Rb) Perovskite Nanocrystals. *J. Phys. Chem. C Nanomater. Interfaces* **2018**, *122* (19), 10643–10649.

(29) Park, B.-W.; Philippe, B.; Zhang, X.; Rensmo, H.; Boschloo, G.; Johansson, E. M. J. Bismuth Based Hybrid Perovskites A3Bi2 I9 (A: Methylammonium or Cesium) for Solar Cell Application. *Adv. Mater.* **2015**, *27* (43), 6806–6813.

(30) Singh, A.; Boopathi, K. M.; Mohapatra, A.; Chen, Y. F.; Li, G.; Chu, C. W. Photovoltaic Performance of Vapor-Assisted Solution-Processed Layer Polymorph of Cs3Sb2I9. *ACS Appl. Mater. Interfaces* **2018**, *10* (3), 2566–2573.

(31) Slavney, A. H.; Hu, T.; Lindenberg, A. M.; Karunadasa, H. I. A Bismuth-Halide Double Perovskite with Long Carrier Recombination Lifetime for Photovoltaic Applications. *J. Am. Chem. Soc.* **2016**, *138* (7), 2138–2141.

(32) McClure, E. T.; Ball, M. R.; Windl, W.; Woodward, P. M. Cs2AgBiX6 (X = Br, Cl): New Visible Light Absorbing, Lead-Free Halide Perovskite Semiconductors. *Chem. Mater.* **2016**, *28* (5), 1348–1354.

(33) Du, K.-Z.; Meng, W.; Wang, X.; Yan, Y.; Mitzi, D. B. Bandgap Engineering of Lead-Free Double Perovskite Cs2 AgBiBr6 through Trivalent Metal Alloying. *Angew. Chem. Int. Ed Engl.* **2017**, *56* (28), 8158–8162.

(34) Li, Q.; Wang, Y.; Pan, W.; Yang, W.; Zou, B.; Tang, J.; Quan, Z. High-Pressure Band-Gap Engineering in Lead-Free Cs2 AgBiBr6 Double Perovskite. *Angew. Chem. Weinheim Bergstr. Ger.* **2017**, *129* (50), 16185–16189.

(35) Wei, H.; Huang, J. Halide Lead Perovskites for Ionizing Radiation Detection. *Nat. Commun.* **2019**, *10* (1), 1066.

(36) Green, M. A.; Jiang, Y.; Soufiani, A. M.; Ho-Baillie, A. Optical Properties of Photovoltaic Organic-Inorganic Lead Halide Perovskites. *J. Phys. Chem. Lett.* **2015**, *6* (23), 4774–4785.

(37) Gao, X.; Zhang, X.; Yin, W.; Wang, H.; Hu, Y.; Zhang, Q.; Shi, Z.; Colvin, V. L.; Yu, W. W.; Zhang, Y. Ruddlesden-Popper Perovskites: Synthesis and Optical Properties for Optoelectronic Applications. *Adv. Sci. (Weinh.)* **2019**, *6* (22), 1900941.

(38) Giovanni, D. Optical-Spin Dynamics in Organic-Inorganic Hybrid Lead Halide Perovskites, Nanyang Technological University, 2020.

(39) Xiao, Z.; Yan, Y. Progress in Theoretical Study of Metal Halide Perovskite Solar Cell Materials. *Adv. Energy Mater.* **2017**, *7* (22), 1701136.

(40) Yang, W. S.; Park, B.-W.; Jung, E. H.; Jeon, N. J.; Kim, Y. C.; Lee, D. U.; Shin, S. S.; Seo, J.; Kim, E. K.; Noh, J. H.; Seok, S. I. Iodide Management in Formamidinium-Lead-Halide–Based Perovskite Layers for Efficient Solar Cells. *Science* **2017**, *356* (6345), 1376–1379.

(41) Hu, J.; Yan, L.; You, W. Two-Dimensional Organic-Inorganic Hybrid Perovskites: A New Platform for Optoelectronic Applications. *Adv. Mater.* **2018**, *30* (48), e1802041.

(42) Mao, L.; Stoumpos, C. C.; Kanatzidis, M. G. Two-Dimensional Hybrid Halide Perovskites: Principles and Promises. *J. Am. Chem. Soc.* **2019**, *141* (3), 1171–1190.

(43) Zheng, Y.; Niu, T.; Ran, X.; Qiu, J.; Li, B.; Xia, Y.; Chen, Y.; Huang, W. Unique Characteristics of 2D Ruddlesden–Popper (2DRP) Perovskite for Future Photovoltaic Application. *J. Mater. Chem. A Mater. Energy Sustain.* **2019**, *7* (23), 13860–13872.

(44) World Economic Forum – Global Risks 2013 eighth edition https://www.weforum.org/reports/world-economic-forum-global-risks-2013-eighth-edition (accessed Apr 26, 2021).

(45) Martin, S. T.; Herrmann, H.; Choi, W.; Hoffmann, M. R. Time-Resolved Microwave Conductivity. Part 1.—TiO2photoreactivity and Size Quantization. *J Chem Soc Faraday Trans* **1994**, *90* (21), 3315–3322.

(46) Martin, S. T.; Herrmann, H.; Hoffmann, M. R. Time-Resolved Microwave Conductivity. Part 2.—Quantum-Sized TiO2and the Effect of Adsorbates and Light Intensity on Charge-Carrier Dynamics. *J Chem Soc Faraday Trans* **1994**, *90* (21), 3323–3330.

(47) Linsebigler, A. L.; Lu, G.; Yates, J. T., Jr. Photocatalysis on TiO2 Surfaces: Principles, Mechanisms, and Selected Results. *Chem. Rev.* **1995**, *95* (3), 735–758.

(48) Ni, M.; Leung, M. K. H.; Leung, D. Y. C.; Sumathy, K. A Review and Recent Developments in Photocatalytic Water-Splitting Using TiO2 for Hydrogen Production. *Renew. Sustain. Energy Rev.* **2007**, *11* (3), 401–425.

(49) Nakata, K.; Ochiai, T.; Murakami, T.; Fujishima, A. Photoenergy Conversion with TiO2 Photocatalysis: New Materials and Recent Applications. *Electrochim. Acta* **2012**, *84*, 103–111.

(50) Kamachimudali, U and Sridhar, TM and Raj, B and Philip, J and Karthikeyan, NR and Banerjee, S and Gopal, J and Muraleedharan, P and Tyagi, AK and Shima, PD and others. Citation Report of Dr. Baldev Raj. *Journal of Alloys and Compounds* **2017**, *696*, 185–192.

(51) Hoffmann, M. R.; Martin, S. T.; Choi, W.; Bahnemann, D. W. Environmental Applications of Semiconductor Photocatalysis. *Chem. Rev.* **1995**, *95* (1), 69–96.

(52) Aliah, H.; Setiawan, A.; Masturi, M.; Abdullah, M. Design of Thermal Equipment Milling for Fabricating the Tio2 Photocatalysts Coated Grain Polymers. *J. pendidik. fis. Indones.* **2015**, *11* (2), 186–192.

(53) Riegel, G.; Bolton, J. R. Photocatalytic Efficiency Variability in TiO2 Particles. *J. Phys. Chem.* **1995**, *99* (12), 4215–4224.

(54) Grela, M. A.; Coronel, M. E. J.; Colussi, A. J. Quantitative Spin-Trapping Studies of Weakly Illuminated Titanium Dioxide Sols. Implications for the Mechanism of Photocatalysis. *J. Phys. Chem.* **1996**, *100* (42), 16940–16946.

(55) Nakamura, R.; Nakato, Y. Molecular Mechanism of Water Oxidation Reaction at Photo-Irradiated TiO_2 and Related Metal Oxide Surfaces. *Solid State Phenom.* **2010**, *162*, 1–27.

(56) Murakami, Y.; Endo, K.; Ohta, I.; Nosaka, A. Y.; Nosaka, Y. Can OH Radicals Diffuse from the UV-Irradiated Photocatalytic TiO2Surfaces? Laser-Induced-Fluorescence Study. *J. Phys. Chem. C Nanomater. Interfaces* **2007**, *111* (30), 11339–11346.

(57) Fujishima, A.; Zhang, X.; Tryk, D. TiO2 Photocatalysis and Related Surface Phenomena. *Surf. Sci. Rep.* **2008**, *63* (12), 515–582.

(58) Wang, S.; Ang, H. M.; Tade, M. O. Volatile Organic Compounds in Indoor Environment and Photocatalytic Oxidation: State of the Art. *Environ. Int.* **2007**, *33* (5), 694–705.

(59) Cavicchioli, A.; Gutz, I. G. R. Effect of Scavengers on the Photocatalytic Digestion of Organic Matter in Water Samples Assisted by TiO2 in Suspension for the Voltammetric Determination of Heavy Metals. *J. Braz. Chem. Soc.* **2002**, *13* (4), 441–448.

(60) Schneider, J. T.; Firak, D. S.; Ribeiro, R. R.; Peralta-Zamora, P. Use of Scavenger Agents in Heterogeneous Photocatalysis: Truths, Half-Truths, and Misinterpretations. *Phys. Chem. Chem. Phys.* **2020**, *22* (27), 15723–15733.

(61) Liu, T.; Wang, L.; Lu, X.; Fan, J.; Cai, X.; Gao, B.; Miao, R.; Wang, J.; Lv, Y. Comparative Study of the Photocatalytic Performance for the Degradation of Different Dyes by ZnIn2S4: Adsorption, Active Species, and Pathways. *RSC Adv.* **2017**, *7* (20), 12292–12300.

(62) Fakhrul Ridhwan Samsudin, M.; Tau Siang, L.; Sufian, S.; Bashiri, R.; Muti Mohamed, N.; Mahirah Ramli, R. Exploring the Role of Electron-Hole Scavengers on Optimizing the Photocatalytic Performance of BiVO4. *Mater. Today* **2018**, *5* (10), 21703–21709.

(63) Mao, C.-Y.; Liao, W.-Q.; Wang, Z.-X.; Li, P.-F.; Lv, X.-H.; Ye, H.-Y.; Zhang, Y. Structural Characterization, Phase Transition and Switchable Dielectric Behaviors in a New Zigzag Chain Organic-Inorganic Hybrid Compound: [C3H7NH3]2SbI5. *Dalton Trans.* **2016**, *45* (12), 5229–5233.

(64) Liao, Q.; Chen, J.; Zhou, L.; Wei, T.; Zhang, L.; Chen, D.; Huang, F.; Pang, Q.; Zhang, J. Z. Bandgap Engineering of Lead-Free Double Perovskite Cs2AgInCl6 Nanocrystals via Cu2+-Doping. *J. Phys. Chem. Lett.* **2020**, *11* (19), 8392–8398.

(65) Karmakar, A.; Dodd, M. S.; Agnihotri, S.; Ravera, E.; Michaelis, V. K. Cu(II)-Doped Cs2SbAgCl6 Double Perovskite: A Lead-Free, Low-Bandgap Material. *Chem. Mater.* **2018**, *30* (22), 8280–8290.

(66) Ashitha; Joshi, M.; Verma, D.; Jadhav, S.; Choudhury, A. R.; Jana, D. Layered Cs4CuSb2Cl12 Nanocrystals for Sunlight-Driven Photocatalytic Degradation of Pollutants. *ACS Appl. Nano Mater.* **2021**, *4* (2), 1305–1313.

(67) Chen, W.; Shi, T.; Du, J.; Zang, Z.; Yao, Z.; Li, M.; Sun, K.; Hu, W.; Leng, Y.; Tang, X. Highly Stable Silica-Wrapped Mn-Doped CsPbCl3 Quantum Dots for Bright White Light-Emitting Devices. *ACS Appl. Mater. Interfaces* **2018**, *10* (50), 43978–43986.

(68) Volonakis, G.; Haghighirad, A. A.; Milot, R. L.; Sio, W. H.; Filip, M. R.; Wenger, B.; Johnston, M. B.; Herz, L. M.; Snaith, H. J.; Giustino, F. Cs2InAgCl6: A New Lead-Free Halide Double Perovskite with Direct Band Gap. *J. Phys. Chem. Lett.* **2017**, *8* (4), 772–778.

(69) Balkus, K. J., Jr. Metal Oxide Nanotube, Nanorod, and Quantum Dot Photocatalysis. In *New and Future Developments in Catalysis*; Suib, S. L., Ed.; Elsevier, 2013; pp 213–244.

(70) Gorasiya, A.; Saha, S. K. Single Phase Laminar Fluid Flow and Heat Transfer in Microchannel with Cylindrical and Parallelepiped Micro-Fins. *Heat Mass Transf.* **2019**, *55* (3), 613–626.

(71) Stoumpos, C. C.; Cao, D. H.; Clark, D. J.; Young, J.; Rondinelli, J. M.; Jang, J. I.; Hupp, J. T.; Kanatzidis, M. G. Ruddlesden–Popper Hybrid Lead Iodide Perovskite 2D Homologous Semiconductors. *Chem. Mater.* **2016**, *28* (8), 2852–2867.

(72) Sheikh, T.; Shinde, A.; Mahamuni, S.; Nag, A. Possible Dual Bandgap in (C4H9NH3)2PbI4 2D Layered Perovskite: Single-Crystal and Exfoliated Few-Layer. *ACS Energy Lett.* **2018**, *3* (12), 2940–2946.

(73) Pradeeba, S. J.; Sampath, K. A COMPARATIVE STUDY OF PHOTOCATALYTIC DEGRADATION EFFICIENCY OF METHYLENE BLUE DYE IN WASTE WATER USING POLY(AZOMETHINE)/ZnO NANOCOMPOSITE AND POLY(AZOMETHINE)/TiONANOCOMPOSITE https://chalcogen.ro/243_PradeebaSJ.pdf (accessed Apr 26, 2021).

(74) Hutter, E. M.; Gélvez-Rueda, M. C.; Osherov, A.; Bulović, V.; Grozema, F. C.; Stranks, S. D.; Savenije, T. J. Direct-Indirect Character of the Bandgap in Methylammonium Lead Iodide Perovskite. *Nat. Mater.* **2017**, *16* (1), 115–120.

(75) Ajmal, A.; Majeed, I.; Malik, R. N.; Idriss, H.; Nadeem, M. A. Principles and Mechanisms of Photocatalytic Dye Degradation on TiO2based Photocatalysts: A Comparative Overview. *RSC Adv.* **2014**, *4* (70), 37003–37026.

(76) Bhoi, Y. P.; Pradhan, S. R.; Behera, C.; Mishra, B. G. Visible Light Driven Efficient Photocatalytic Degradation of Congo Red Dye Catalyzed by Hierarchical CuS–Bi2CuxW1−xO6−2x Nanocomposite System. *RSC Adv.* **2016**, *6* (42), 35589–35601.

(77) Malwal, D.; Gopinath, P. Enhanced Photocatalytic Activity of Hierarchical Three Dimensional Metal Oxide@CuO Nanostructures towards the Degradation of Congo Red Dye under Solar Radiation. *Catal. Sci. Technol.* **2016**, *6* (12), 4458–4472.

(78) Czili, H.; Horváth, A. Applicability of Coumarin for Detecting and Measuring Hydroxyl Radicals Generated by Photoexcitation of TiO2 Nanoparticles. *Appl. Catal. B* **2008**, *81* (3–4), 295–302.

(79) Dutta, S. K.; Dutta, A.; Das Adhikari, S.; Pradhan, N. Doping Mn2+ in Single-Crystalline Layered Perovskite Microcrystals. *ACS Energy Lett.* **2019**, *4* (1), 343–351.

(80) Zhou, G.; Guo, S.; Zhao, J.; Molokeev, M.; Liu, Q.; Zhang, J.; Xia, Z. Unraveling the Mechanochemical Synthesis and Luminescence in MnII-Based Two-Dimensional Hybrid Perovskite (C4H9NH3)2PbCl4. *Sci. China Mater.* **2019**, *62* (7), 1013–1022.

(81) Xiao, Z.-L.; Chen, H.-Z.; Shi, M.-M.; Wu, G.; Zhou, R.-J.; Yang, Z.-S.; Wang, M.; Tang, B.-Z. Preparation and Characterization of Organic–Inorganic Hybrid Perovskite (C4H9NH3)2CuCl4. *Mater. Sci. Eng. B Solid State Mater. Adv. Technol.* **2005**, *117* (3), 313–316

(82) Gaya, U. I.; Abdullah, A. H. Heterogeneous Photocatalytic Degradation of Organic Contaminants over Titanium Dioxide: A Review of Fundamentals, Progress and Problems. *J. Photochem. Photobiol. C: Photochem. Rev.* **2008**, *9* (1), 1–12.

(83) Zhang, Z.; Liang, Y.; Huang, H.; Liu, X.; Li, Q.; Chen, L.; Xu, D. Stable and Highly Efficient Photocatalysis with Lead-Free Double-Perovskite of Cs2 AgBiBr6. *Angew. Chem. Int. Ed Engl.* **2019**, *58* (22), 7263–7267.